Electron-Photon Quantum State Heralding Using Photonic Integrated Circuits

Guanhao Huang,[1,2,*] Nils J. Engelsen,[1,2] Ofer Kfir,[3] Claus Ropers,[4,5] and Tobias J. Kippenberg[1,2]

[1] *Swiss Federal Institute of Technology Lausanne (EPFL), Lausanne CH-1015, Switzerland*
[2] *Center for Quantum Science and Engineering, EPFL, Lausanne CH-1015, Switzerland*
[3] *School of Electrical Engineering, Tel Aviv University, Tel Aviv 69978, Israel*
[4] *Max Planck Institute for Multidisciplinary Sciences, Göttingen D-37077, Germany*
[5] *Georg-August-Universität Göttingen, Göttingen D-37077, Germany*

(Received 20 June 2022; revised 24 February 2023; accepted 1 June 2023; published 26 June 2023)

Recently, integrated photonic circuits have brought new capabilities to electron microscopy and been used to demonstrate efficient electron phase modulation and electron-photon correlations. Here, we quantitatively analyze the feasibility of high-fidelity and high-purity quantum state heralding using a free electron and a photonic integrated circuit with parametric coupling, and propose schemes to shape useful electron and photonic states in different application scenarios. Adopting a dissipative quantum electrodynamics treatment, we formulate a framework for the coupling of free electrons to waveguide spatial-temporal modes. To avoid multimode-coupling-induced state decoherence, we show that with proper waveguide design, the interaction can be reduced to a single-mode coupling to a quasi-TM_{00} mode. In the single-mode coupling limit, we go beyond the conventional state ladder treatment, and show that the electron-photon energy correlations within the ladder subspace can still lead to a fundamental purity and fidelity limit on complex optical and electron state preparations through heralding schemes. We propose applications that use this underlying correlation to their advantage, but also show that the imposed limitations for general applications can be overcome by using photonic integrated circuits with an experimentally feasible interaction length, showing its promise as a platform for free-electron quantum optics.

DOI: 10.1103/PRXQuantum.4.020351

Quantum coherent coupling between distinct physical systems harnesses the advantages and strengths of the different systems in order to better explore new phenomena and potentially develop novel quantum technologies [1,2]. Photonic links [3] are most commonly used to connect different systems due to the potential for long-range transmission through optical fibers and robustness to decoherence from thermal environments, and have been realized in systems ranging from superconducting qubits [4,5], solid-state spins [6,7], ultracoherent mechanics [8,9], and atomic systems [10–14], where each offers unique features and advantages to be utilized in a hybrid quantum system. One key aspect of all these systems is the ability to enact high-fidelity quantum control of the interaction with well-defined optical modes.

In the field of electron microscopy, interactions between free electrons and photons have been widely explored in both stimulated [15–27] and spontaneous processes [17,28–30] enhanced by phase-matched interactions and optical resonances [31–36]. There have also been many proposals that explore the unique quantum properties of electron-photon states [37–41]. However, it is still an open question whether high-fidelity quantum control of this hybrid quantum system can be realized.

High-fidelity quantum control requires high coupling strength between free electrons and optical vacuum fields, and low dissipation to keep decoherence at a minimum. The interaction mechanisms and their coupling strengths differ substantially between different physical platforms, which can be categorized into metallic [21] and dielectric structures [19,20,24,25,31,35,42,43]. For nanophotonic particles, the short attosecond-long interaction time promotes the use of dissipative materials, such as plasmonic structures [44]. The collective electronic response amplifies the interaction, while at the same time bringing retardation and dissipation, which is not ideal for quantum coherent manipulation of electrons with optical states. On the other hand, transparent dielectrics, for which the coupling is enhanced by an extended interaction length,

*guanhao.huang@epfl.ch

offer a paradigm shift in free-electron quantum optics due to their low optical dissipation and practically instant electronic response. Instead of enhancing the interaction by lossy media, optical modes supported by dielectric structures interact with the free electron by a geometric effect through the relativistic field retardation [45], which results in a purely parametric interaction ideally suited for high-fidelity quantum control.

Photonic integrated circuits have only entered the picture very recently [35,46], and have several advantages for free-electron quantum optical experiments. Firstly, integrated photonics enables exquisite control of the optical properties of waveguides [47,48]. The nearly lossless guided modes [49] and high-efficiency output fiber coupling [50] facilitate coupling to both on-chip [6–9] and fiber-coupled quantum systems [4,11–14]. Additional capabilities are provided by well-established on-chip optical elements such as tunable beam splitters and phase shifters [51], spectral filters [52], and photon counters [53], which offer high-fidelity optical state manipulation and characterization [54]. With the versatile on-chip structures and demonstrated efficient electron phase modulation [35] and electron-photon correlation [46], we propose heralding schemes to shape useful electron [40] and optical states [39,41,55] in various application scenarios with photonic integrated circuits.

To transfer the aforementioned advantages to the scenario of generating high-quality quantum states through electron-photon interaction, high-ideality coupling to a single well-defined optical mode [56] is required. However, due to the complex waveguide structures, parasitic couplings to auxiliary spatial modes cause decoherence of the system, see Fig. 1(a). We quantitatively investigate this limitation in a realistic experimental scenario, and show that with a single-mode waveguide, larger gap distance, and long interaction length, near-unity coupling ideality and strong coupling [37,57] can be achieved to the waveguide quasi-TM_{00} spatial-temporal mode.

Further, we show that even in the limit of single-mode interaction, there is still a state subspace correlation that imposes a fundamental limit to the state fidelity and purity. To address the electron-photon interaction in the conventional quantum optics description, a synthetic ladder-state space [23,37–41] is usually used, shown in Fig. 1(b). This treatment greatly eases the analysis of the interaction between two systems that are actually continuum systems. However, within the subspace of a ladder level, energy conservation enforces strong correlation between the electron energy loss and the frequency of the photon created. When one neglects the underlying correlation, information loss occurs. This process can be characterized by the state purity, that captures both the distance to a pure quantum state, and the degree of electron-photon entanglement through Rényi-2 entropy [58]. Here, we

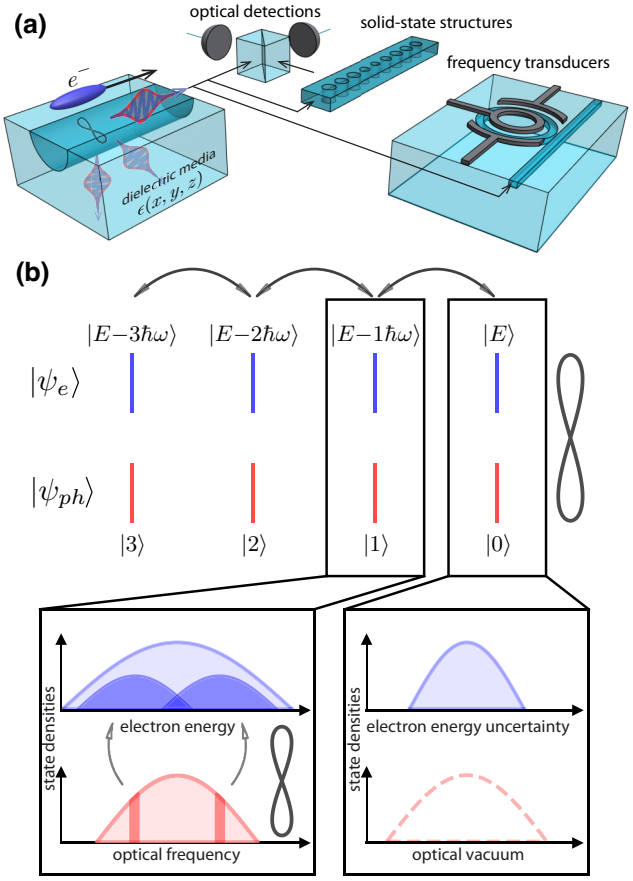

FIG. 1. (a) Illustration of the electron-photon inelastic scattering process mediated by a dielectric waveguide. In an electron microscope, when the high-energy electron passes by a dielectric waveguide structure with a given dielectric permittivity distribution $\epsilon(x,y,z)$, the material dielectric dipoles exert a backaction field (force) on the electron, resulting in correlated electron energy loss and optical emission in both the guided waveguide modes and nonguided bulk modes. High-ideality coupling to a low-loss waveguide mode is required for high-fidelity state preparation and interaction with other quantum systems through optical links. (b) Synthetic electron-photon state ladder of the pair-state generation through $\hat{S}_{e\text{-ph}}$. Within each ladder state, there is an underlying subspace that still maintains correlation between electron energy and photon frequencies. For any two optical frequency components (shown in dark red), the correlated electron energy states (shown in dark blue) are only partially degenerate. This correlation can lead to new types of applications, but generally leads to degradation of fidelity and purity of the interaction.

propose applications that exploit this underlying correlation to their advantage, e.g., imprinting electron wave functions onto optical states, and later examine the state fidelity and purity in quantum state heralding schemes. We find that electrons in particlelike states with high purity are required to generate pure heralded states, and the purity limits are greatly reduced with experimentally feasible interaction length using photonic integrated circuits.

The paper is organized as follows: Sec. I establishes the theoretical formalism for describing electron-photon spontaneous scattering processes with dielectric media, different parameter regimes, and the underlying state correlations within the energy ladders. Section II studies the interaction in a photonic integrated circuit structure, defines the spatial-temporal modes and provides guidelines to achieve single-mode coupling. Section III investigates optical state heralding in wavelike and particlelike regimes, shows corresponding applications and quantitative analysis of the correlation-induced state heralding fidelity and purity limit. Section IV investigates electron state heralding schemes, optical mode matching, and down-conversion schemes, and the state purity limit. Section V summarizes the paper, discussing the theoretical limitations of our analysis and the experimental constraints.

I. ELECTRON-PHOTON INTERACTIONS WITH DIELECTRIC MEDIA

The interaction between free electrons and optical modes at a dielectric surface can be understood in a microscopic picture as follows: when an electron passes near the surface of a dielectric structure, the electric field of the flying electron polarizes the dipoles in the structure [see Fig. 1(a)]. As a result, these dipoles generate oscillating electromagnetic fields that cause backaction Coulomb forces on the electron, which change the electron energy. In the conventional quantum optical modal decomposition picture commonly used in the cavity quantum electrodynamics (QED) community, this can be interpreted as the interaction between the free electrons and the optical vacuum fields of the modes supported by the dielectric structure [59].

Here, we formulate the problem as the interaction between propagating free electrons and one single interaction-specific optical spatial mode $\hat{\mathbf{A}}(\mathbf{r},\omega)$ (see Appendix A for the QED details and the field profile) at frequencies ω in the continuum, instead of predetermined discrete optical modes of the dielectric structure (see Appendix C for its correspondence to modal decomposition), with the scattering matrix [37,56] in the interaction picture

$$\hat{S}_{e\text{-ph}} = e^{i\hat{\chi}} \exp\left[\int d\omega g_\omega \hat{b}_\omega^\dagger \hat{a}_\omega - \text{h.c.}\right], \tag{1}$$

where the phase operator $\hat{\chi}$ acts only on the electron degrees of freedom (ignored in the remaining discussion), and is associated with the Aharonov-Bohm effect of the vector potential [60]. Continuum photon ladder operators $\hat{a}_\omega$ and electron operators $\hat{b}_\omega$ characterize the energy exchanges between the electron and the optical field at a given optical frequency ω in an energy-conserving manner. The interaction with the vacuum optical fields results in transitions into lower electron energy states with energy differences of $\hbar\omega$. We define the electron-photon coupling strength at a given photon energy $\hbar\omega$ in terms of the vacuum coupling strength g_ω as $\Gamma(\omega) = |g_\omega|^2$ [17]. The phase-matching condition gives the vacuum coupling strength a finite bandwidth. In the limit where $\Gamma(\omega) \ll 1$, $\Gamma(\omega)$ is equivalent to the electron energy-loss probability per unit optical frequency of dielectric media measured in electron energy-loss spectroscopy (EELS), and can be derived classically in a simplified picture (see Appendix B). To simplify the discussion here, we also assume a pointlike transverse distribution for the electron (see Appendix A for the discussion on the transverse effect), and the vacuum coupling strength g_ω is derived at a corresponding transverse position $\mathbf{R}_0$.

The interaction with the optical continuum, as opposed to the conventional discrete energy-ladder levels illustrated in Fig. 1(b), results in a continuum electron-photon pair state

$$|\psi_e, \psi_{\text{ph}}\rangle = \exp\left(-\frac{\int d\omega |g_\omega|^2}{2}\right) \times \left(\sum_N \frac{\left(-\int d\omega g_\omega^* \hat{b}_\omega \hat{a}_\omega^\dagger\right)^N}{N!} \int dE \psi(E) |E\rangle|0\rangle\right), \tag{2}$$

where $\psi(E)$ is the electron wave function in the energy domain. We show in Fig. 2 that depending on the size of the electron wavepacket [61–63], the electron-photon interaction can be categorized into three regimes. The classical regime has been explored [39,55], and is accessible through laser modulation schemes [23,40,64–66]. Some electron microscopes equipped with a monochromator fall into the wavelike regime[33,67], while others with longer interaction length [46] are in an intermediate wave-particle-like regime. The simplified electron-photon ladder picture is only partially valid in both cases.

In the wave-particle-like regime, the ladder state $|\psi_e, \psi_{\text{ph}}\rangle_N \propto \int dE \psi(E) \left(\int d\omega g_\omega^* \hat{b}_\omega \hat{a}_\omega^\dagger\right)^N |E\rangle|0\rangle$ maintains a correlation between electron energies E and photon frequencies ω. To go back to the simplified ladder picture, one traces out, e.g., the continuum electron states within each ladder as $\hat{\rho}_{\text{ph},N} = \text{Tr}_E\left[|\psi_e, \psi_{\text{ph}}\rangle_N \langle\psi_e, \psi_{\text{ph}}|_N\right]$, which results in a degradation of the optical state purity $\mathcal{P} = \text{Tr}\left[\hat{\rho}_{\text{ph},N}^2\right]$. To reduce the degree of correlation and reach the particlelike regime, a narrower phase-matching bandwidth relative to the electron energy uncertainty is generally required.

We show in the latter half of this paper that in the case of photonic integrated circuits, the prolonged interaction

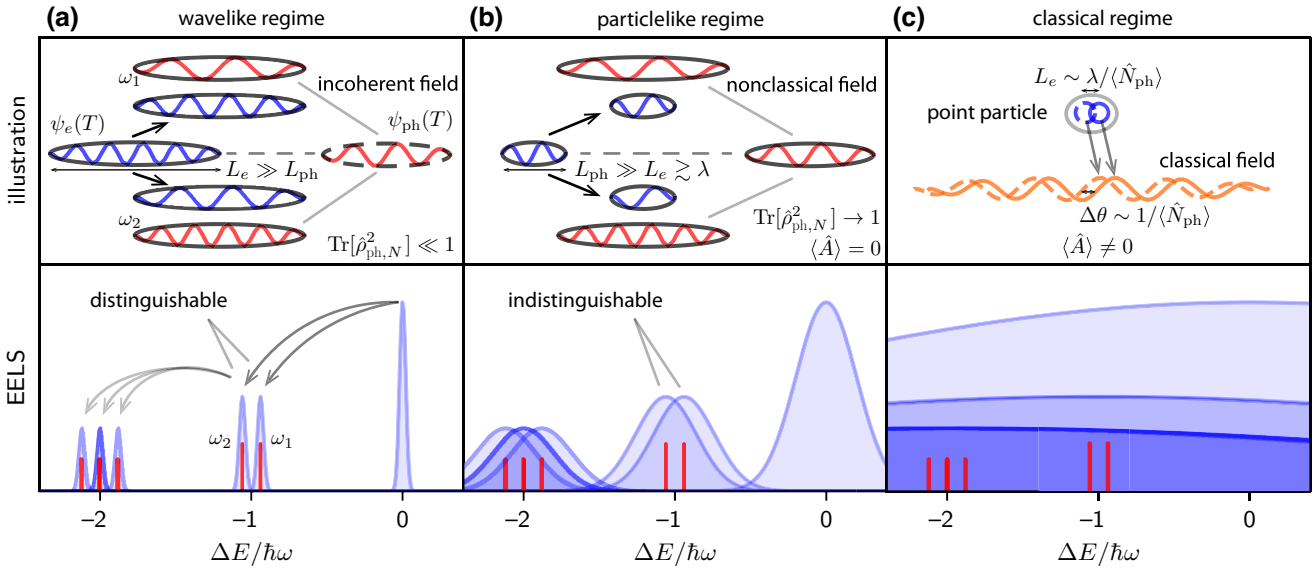

FIG. 2. Illustration of different parameter regimes of electron-photon interactions. The electron (blue) and photon (red or orange) spatial waveforms as a function of $T = t - z/v_e$, where z is the longitudinal coordinate, are shown in the upper panels, and the corresponding energy (frequency) domain picture is shown in the lower panels. The frequency bandwidth of the generated photon is determined by the phase-matching mechanism, and two of the frequency components (ω_1, ω_2), together with their correlated electron states, are shown in both the spatial and energy domain representations to illustrate the qualitative differences between different regimes. The arrows in the panels indicate the direction of the scattering processes. (a) Wavelike regime where distinguishable electron states are generated from the emission of photons with the corresponding frequencies. As a result, the optical frequency components cannot be coherently combined to form a single-mode field. Therefore, this regime is accompanied by mixed optical ladder states $\rho_{\mathrm{ph},N}$, and incoherent photon emission. (b) Particlelike regime where the photon emission at different frequencies generates indistinguishable electron states. The optical state space is sufficiently decoupled from the electron state space, and can be described as a single-mode field. This regime has pure optical ladder states $\rho_{\mathrm{ph},N}$, where the synthetic electron-photon state ladder is a valid approximation. (c) Classical regime where different photon sidebands of the electron overlap well, and classical optical field emission with nonzero $\langle\hat{A}\rangle$ is achieved. In the spatial representation, the classical waves are plotted orange to distinguish it from the quantum counter parts in the other regimes.

length can help reduce the phase-matching bandwidth and lower the energy correlation for a single waveguide mode, pushing the system parameters well into the particlelike regime. However, the complex dielectric environment generally results in multimode electron-photon interactions, e.g., through parasitic coupling to other optical mode families and other nonguided spatial modes supported by open-ended dielectric substrates. The effective phase-matching bandwidth of the multimode coupling is generally large, and the corresponding electron-photon correlation cannot be suppressed by a longer interaction length. Therefore, we first quantitatively analyze how to effectively constrain the interaction to the single-mode case.

It is generally hard to design and fabricate waveguide structures that achieve 100% spatial overlap between a waveguide mode and the electron optical emission over the full optical frequency range. Therefore, instead of mode-matching, our strategy to achieve single-mode interaction is to exploit a combination of effects, which are results of the phase-matching mechanism.

To quantitatively account for the infinite number of interacting spatial optical modes, it is generally impractical to use the conventional modal decomposition method [21]. Instead, as is mentioned before, we combine all the possible coupling contributions from different modes into one single interaction-specific spatial mode, following a three-dimensional QED treatment [68]. This formalism, derived using the fluctuation-dissipation theorem, was previously used when analyzing electron energy-loss probabilities with dissipative materials [17] that exhibit a delayed material response, which is the dominant contribution to the main electron energy-loss channels. The dielectric materials we study here are transparent in the optical frequency bands of interest. In this sense, we can set $\mathrm{Im}\{\epsilon(\mathbf{r},\omega)\} \to 0$, which corresponds to an instantaneous dielectric dipole response and further simplifies the analysis. For materials with sufficiently low absorption, which are used for integrated waveguides designed to guide optical fields, the interaction is purely contributed from the relativistic field retardation effect [45] and prohibits energy and momentum transfer to the material, avoiding loss of coherence. It is in this sense that the whole process of an electron interacting with dielectric waveguide is *parametric* in nature.

II. COUPLING IDEALITY

In this section, we show how to achieve ideal single-mode electron-photon coupling with photonic integrated circuits. As an example, here we quantitatively investigate the electron-photon coupling mediated by an integrated Si_3N_4 waveguide embedded in a silica substrate without top cladding (the bottom silicon substrate is not considered), shown in Fig. 3(a). This type of structure has been used in recent investigations of both stimulated phase-matched interactions [35] and spontaneous inelastic scattering [46] between free electrons and the evanescent field of a photonic-chip-based optical microresonator, and features ultralow material-limited loss of 0.15 dB/m [49]. We calculate the electron-photon vacuum coupling strength (numerical details in Appendix D) and plot it in Figs. 3(b) and 3(c) as a function of electron velocity for optical wavelengths ranging from 780 nm to 2.5 μm (where all relevant material properties are well known), which covers most of the frequency bands that are of general interest.

Under the optimal phase-matching condition, the interaction strength of the waveguide transverse modes scales quadratically with respect to the interaction length since they co-propagate with the electron, in contrast to the linear relation of bulk modes. In reality, waveguide-mode phase velocity differs at different optical frequencies. Through the phase-matching mechanism, linear chromatic dispersion limits the coupling bandwidths to scale inversely proportional to the interaction length. With prolonged interaction length, coupling strengths to different waveguide transverse mode families are isolated in optical frequencies, and exhibit peak features shown in Figs. 3(b) and 3(c). Dispersion-free systems are generally feasible in higher dimensions and have been realized in specially structured photonic lattices [69–71], where the optical modes of interest are generally unguided. In integrated photonics, advances in dispersion engineering have enabled waveguide designs that tailor the modal dispersion [48,72], promising dispersion-free quadratic coupling enhancement over a broad frequency range. In our study, we focus on translation-invariant straight waveguides, which exhibit chromatic dispersion determined by the waveguide materials and geometry.

The waveguide mode families have finite coupling bandwidths and are well isolated from each other. We therefore define discrete spatial-temporal optical modes $\hat{a}_m \propto \int d\omega g_{m,\omega}\hat{a}_\omega$ associated with different waveguide mode families from the optical continuum based on the vacuum coupling strengths $g_{m,\omega}$ of the interaction (details see Appendix C). The coupling strength of a given mode family $\hat{a}_m$,

$$|g_m|^2 = \int d\omega |g_{\omega,m}|^2, \tag{3}$$

scales linearly with interaction length and inversely with chromatic dispersion. We quantitatively evaluate the coupling strengths $|g_m|^2$ to different spatial-temporal modes $\hat{a}_m$ based on the fitted interaction strength $|g_{m,\omega}|^2$ from the simulation results. As an example, for the quasi-TM_{00} mode of the 800-nm-wide waveguide shown in Fig. 3(c), for an electron-waveguide gap of 100 nm, a strong coupling strength [37,57] of $|g_{TM_{00}}|^2 \sim 1$ can be achieved with 200 μm of interaction length at an electron velocity of $v_e/c = 0.65$ (a kinetic energy of 160 keV). A 100-nm gap and a 100-μm length of electron-beam propagation is experimentally feasible and demonstrated in Ref. [46] with a gradient $d|g_{TM_{00}}|^2/dz \sim 5\ \mathrm{mm}^{-1}$.

Using the procedure described in the previous paragraph, we quantitatively investigate the influence of competing waveguide modes for a given waveguide configuration, and how one can approach unity coupling ideality by a

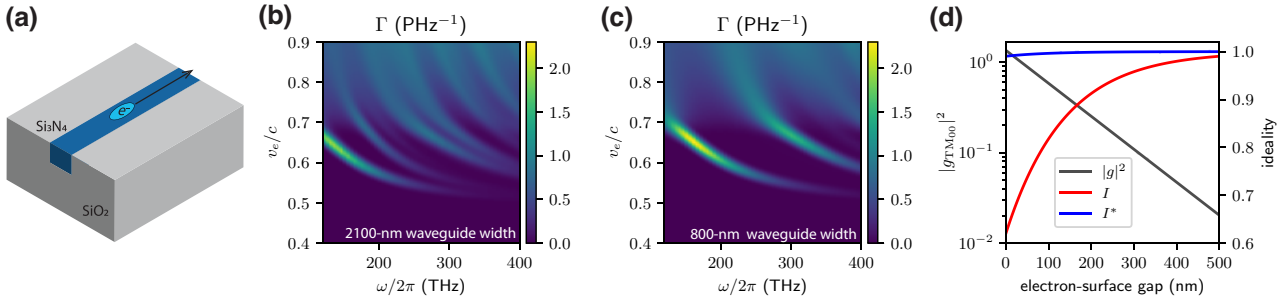

FIG. 3. (a) Illustration of the waveguide structure studied, consisting of a Si_3N_4 waveguide embedded in a silica substrate. The free electron passes by the top surface of the waveguide and generates correlated optical emission. (b),(c) Electron-photon coupling strength $\Gamma(\omega)$ spectrum for different waveguide geometries and electron positioning. The coupling spectrum is plotted as a function of both electron velocity v_e and optical frequency ω. The waveguides have a thickness of 650 nm, and widths of (b) 2.1 μm and (c) 800 nm. Coupling to different waveguide mode families appears as multiple coupling bands, and their phase-matching bandwidth is kept constant for better visualization. (d) Total coupling strength of TM_{00} mode versus nonconditional and conditional coupling idealities (I and I^*, respectively), as a function of gap distance between the electron beam and the waveguide surface, with 800-nm waveguide width, 100-μm interaction length, and $v_e/c = 0.65$ electron velocity.

proper choice of waveguide geometry and material, and electron-beam positioning and velocity. Since the lowest-order TM_{00} mode is generally the most strongly coupled and is the most spectrally isolated mode, we target unity coupling ideality, defined by the coupling fraction

$$I \equiv |g_{TM_{00}}|^2 / \int d\omega |g_\omega|^2, \tag{4}$$

to the TM_{00} mode.

From the numerical result shown in Figs. 3(b) and 3(c), we find that reduced waveguide cross section (to single-mode dimension) enhances the mode index contrast, and results in more spectrally isolated fundamental modes. With a better frequency isolation, the evanescent field of the coupled higher-order modes decay much faster than that of the fundamental mode in the near field, as a result of their higher optical frequencies. Therefore, one can enhance the ideality by increasing the gap distance to the waveguide surface, with $1 - I$ decreasing exponentially with gap distance (details in Appendix D).

In addition to coupling to higher-order waveguide mode families, one can also identify a rising background in the high velocity region. It can be attributed to strong coupling to the substrate modes in the Cherenkov regime ($v \gtrsim 0.7c$), where the charged particle velocity exceeds the phase velocity of light in dielectric media (here: silica). In Appendix E, we quantify the contribution of the substrate bulk modes. This contribution can be suppressed by either choosing an electron velocity well below the Cherenkov regime of the substrate, or by using a low index material as the substrate (e.g., by suspending the structure in vacuum).

Here, we quantitatively analyze the coupling idealities in different application scenarios, and show the results in Fig. 3(d). First, we consider state heralding applications, e.g., heralded single-photon sources by photon-energy loss selection with EELS. We assume an initial electron state with a fitted 0.6-eV Voigt zero-loss-peak (ZLP) profile, and show that by conditioning on the first energy-loss sideband, one can easily achieve more than 99% conditional coupling ideality I^* to the TM_{00} mode outside the Cherenkov regime ($v_e \lesssim 0.7c$) with a single-mode waveguide and the electron beam positioned $\gtrsim 100$ nm above the surface (details in Appendix D). For a general application that is sensitive to the full optical spectrum, we show that more than 95% nonconditional coupling ideality I can be achieved with the electron beam placed $\gtrsim 300$ nm above the surface, limited by the parasitic coupling to the higher-order waveguide modes. This is not a fundamental limitation, as one can always increase the gap distance from the waveguide surface to achieve higher ideality, at the expense of reduced coupling strength. This trade-off is also illustrated in Fig. 3(d), where the total coupling strength $|g_{TM_{00}}|^2$ is plotted against the coupling ideality. However, this effect can generally be compensated with longer interaction length L. As a result, given a fixed waveguide geometry and a target total coupling strength, the deviation from unity is given by $1 - I \propto L^{-1}$.

In the special case where the waveguide loops and forms a resonator, the result of the open-ended waveguide studied here can equally apply (see Appendix F). In most scenarios, where the electron longitudinal spatial wave function is shorter than the cavity round-trip length, or in the frequency-domain picture where the electron zero-loss-peak (ZLP) width is broader than the cavity free-spectral-range, there is no difference in terms of coupling ideality between a straight waveguide and a resonator. The physical picture is that when the emitted optical pulse does not interact with the electron a second time, the emission is only determined by the local structure around the electron, and any nonlocal emission enhancement, e.g., Purcell effect [73] in atom-cavity systems, is absent. In the case of a resonator, the pulse will circulate multiple times and exit the cavity as a pulse train, and exhibit in the frequency domain as a comb structure, as was shown in Refs. [32,33,46].

Note that the experimentally measured ZLP width consists of a coherent energy spread of a single-electron wave function, e.g., inherited from the driving laser pulses in the cold-field electron emission process, and also an incoherent broadening due to, e.g., the statistical imprecision of the electron acceleration voltage and the measurement instrument. In this paper, we mostly use ZLP width to refer to the coherent energy width, unless otherwise specified.

Generally, residual coupling to the higher-order modes can be further mitigated with heralding schemes. As an example, one can place a bandpass spectral filter [52] around the frequency band of the target mode. Upon conditioning on photon-absence events at the dark port of the filter, one can further approach unity ideality, and be eventually limited by the background bulk contribution. As long as the velocity is far from the Cherenkov regime of the substrate material, we estimate this contribution to be far less than 1%. With near-unity coupling ideality, the fidelity and purity of the interaction will be limited to the correlation between electron energy and the optical frequency components of a single spatial-temporal optical mode within the ladder-state space. In the following sections, we discuss this fundamental limitation in the cases of state heralding schemes.

III. SHAPING OPTICAL STATES FROM MEASUREMENT ON ELECTRON ENERGY

In this section, we consider the case of heralding a general optical state by measuring the electron energy. To simplify the discussion here and capture the main features of the physics considered, we assume coupling to a single spatial-temporal optical mode with $I = 1$, and a coherent electron wavefunction $\psi(E)$ prepared before the

interaction. The effect of electron sideband overlaps (with expression shown in Appendix G) is not considered since they can be efficiently eliminated experimentally and are thus not a fundamental limitation.

We first investigate the consequences of electron-photon correlation in the state subspace in some general state-preparation schemes. We consider a projection $\hat{M} = |E_c\rangle\langle E_c|$ on the electron's first photon sideband (general case in Appendix G). This results in a pure single-photon optical state with frequency components $\phi_\omega \propto g^*_\omega \psi(E_c + \hbar\omega)$, a product between the electron wave function and the vacuum coupling strength. This reflects the fact that the electron energy loss is intrinsically correlated with the frequency of the photon created. The strength of the correlation depends on the initial energy uncertainty of the electron, which determines how well the photon frequency components can be distinguished by measurements of the electron state. In a stark contrast, we see in the next section that this is not the case for the electron state heralded by photon counting, since in the no-recoil limit the frequency of the photon created does not depend on the energy of the electron. In this section, we consider two regimes of interest: the wavelike regime (Sec. A) that exploits the correlation to its advantage, and the particlelike regime (Sec. B) that aims for high-purity state heralding.

A. Wavelike regime

In the wavelike regime, the electron ZLP width is much narrower than the phase-matching bandwidth, as shown in Fig. 4(a), where the electron behaves more wavelike to different optical frequency components. This regime exploits the strong correlation in the subspace between electron energy and optical frequency. This is compatible with the experimentally achieved [67] 4-meV ZLP width using a monochromator [33] combined with the recently demonstrated approximately 100-meV phase-matching bandwidth [46]. In this regime, we show the expression for the heralded single-photon Fock state as

$$|\psi_{\rm ph}\rangle \propto \int d\omega \psi(E_c + \hbar\omega)\hat{a}^\dagger_\omega|0\rangle. \tag{5}$$

In this scenario, ignoring the waveguide dispersion during propagation, as well as electron energy dispersion, we effectively imprint the electron spatial wave function $\widetilde{\psi}(T = t - z/v_e)$ onto the optical waveform $\phi(T)$ of

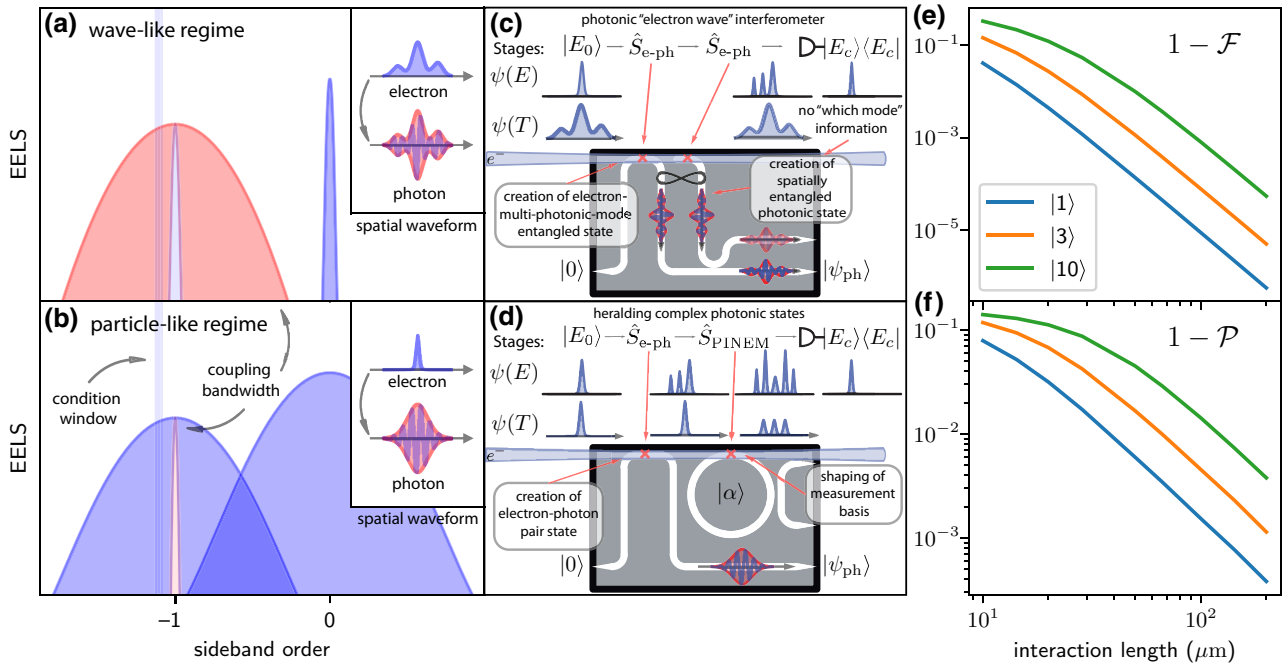

FIG. 4. (a),(b) Shaping optical waveforms by measuring electron energy. In the limit of (a) strong correlation with narrow zero-loss-peak (ZLP, blue) and wide phase-matching bandwidth (red), heralding results in printing electron wave function onto the optical waveform. In the limit of (b) weak correlation with wide ZLP and narrow phase-matching bandwidth, the heralded optical waveform is determined by waveguide routing and material dispersion. (c),(d) Optical state heralding schematics where electron wave functions in time [$\psi(T)$] and energy [$\psi(E)$] domains are drawn before and after interaction stages (marked by red crosses). (c) Scheme for electron-mediated self-mode-matched optical interferometer with nonclassical states, enables measurement of interferometer imbalance to the order of optical wavelength, and electron wave-function tomography. (d) Scheme for heralding a general optical state by measuring electron energy, consisting of one stage for pair-state preparation with $\hat{S}_{\rm e\text{-}ph}$ and one stage for measurement basis selection with $\hat{S}_{\rm PINEM}$. (e),(f) Investigation of subspace correlation-induced degradation of fidelity and purity of different Fock-state components as a function of interaction length.

the generated single-photon Fock state of spatial-temporal mode $\hat{a} \propto \int d\omega \psi^*(E_c + \hbar\omega)\hat{a}_\omega$, with

$$\phi(T) = \widetilde{\psi}(T)e^{i\omega_c T}, \tag{6}$$

with a center frequency $\omega_c = E_c/\hbar$ matching the conditioned electron energy E_c. Therefore, by shaping the electron wave function (e.g., precompression into THz pulse trains) and conditioning on a specific sideband energy, one can transfer the arbitrarily shaped electron spatial wave function to the optical waveform at a desired optical frequency. As for higher-order conditional Fock states $|N\rangle$, they cannot be addressed into the N-photon excitation of a single spatial-temporal mode (see Appendix G) because the optical frequency components are highly correlated, but in any photon-counting scheme, the optical profile is still shaped as $|\phi(T)|^2$ and contains N photons.

We illustrate in Fig. 4(c) an application example in this regime. When an electron passes through two waveguides, and is then measured at the first photon sideband on the detector (single-photon excitation), the measurement does not resolve in which waveguide the photons are created. In this scenario, the measurement creates a spatial entanglement of photon excitation in the two spatially separated waveguides,

$$\hat{S} \propto \int d\omega \psi(E_c + \hbar\omega)\left(\hat{a}^\dagger_{1,\omega} + e^{i\omega\Delta t}\hat{a}^\dagger_{2,\omega}\right) \tag{7}$$

with naturally mode-matched waveform $\phi(T)$ and a controlled phase depending on the effective delay Δt from the electron trajectory, essential for generating path-entangled NOON states [74]. If we interfere the two entangled modes with a balanced beam splitter, there is coherent quantum inference between the two waveguide excitations (see Appendix J). In this way, we effectively construct an optical interferometer with a nonclassical optical state mediated by free electrons, with output differential photon flux

$$f(t) \propto \mathrm{Re}\left[\widetilde{\psi}(t)\widetilde{\psi}^*(t + \Delta t)e^{i\omega_c \Delta t}\right]. \tag{8}$$

Notice that due to the nature of broadband optical coupling, when conditioning on different electron energy E_c, we are effectively scanning the probing optical frequency of the interferometer ω_c, enabling accurate extraction of the time imbalance Δt to the order of only a few optical cycles. When sweeping the optical path-length difference to induce mode mismatch, one can also retrieve electron spectra density based on interference visibility, similar to what was realized in matter interferometers [75]. The electron wave function can also be reconstructed through spectral shearing interferometry [76], answering an important question that is both fundamental and practical: how much of the measured electron energy uncertainty is quantum coherent [63].

B. Particlelike regime

In the particlelike regime, typically associated with a long interaction length, the phase-matching bandwidth is very narrow compared to the electron energy uncertainty and the coupling strength becomes large, as shown in Fig. 4(b). Without on-chip electron guiding structures [36,77], we expect the longest interaction length to be limited to 1 mm with $|g_{\mathrm{TM}_{00}}|^2 \sim 5$ given beam divergence angle approximately 0.2 mrad [78] with a 100-nm gap. The electron behaves more particlelike in this regime, and can hardly distinguish different optical frequency components, therefore, the spatial-temporal optical modes defined in Sec. II can be correctly applied. In this limit, the subspace correlation can be greatly suppressed. When conditioning on the Nth energy sideband, we can simplify the state to photon excitations of an electron-measurement-independent spatial-temporal mode $\hat{a} \propto \int d\omega g_\omega \hat{a}_\omega$ as

$$|\psi_{\mathrm{ph}}\rangle \propto \left(\int d\omega g^*_\omega \hat{a}^\dagger_\omega\right)^N |0\rangle, \tag{9}$$

$$\phi(T) \propto \int dz \widetilde{U}^*_z(z, T), \tag{10}$$

where the optical waveform $\phi(T)$ is connected to the Fourier transform of the optical mode profile $\widetilde{U}_z(z, T) = \mathrm{FT}_\omega[U_z(z, \omega)]$ along the electron propagation trajectory, determined by waveguide routing, and is generally much longer than the spatial extent of the electron wave function. For the case that includes propagation dispersion see Appendix I. Since the electron travels in a straight path, by using a tailormade waveguide structure with proper dispersion and routing, most types of optical waveforms can be generated. The center frequency of the optical excitation is not determined by the conditioned electron energy, but can be easily tuned by selecting the appropriate electron velocity, evident in the results shown in Figs. 3(b) and 3(c).

In the following, we restrict ourselves to the regime of long interaction length, since it is most versatile for heralding more complex optical states with higher photon numbers, and the ladder-subspace correlation is weaker due to narrow phase-matching bandwidth. Heralding optical states by measuring electron energies has been explored [39,41,55], and here we show an example on how to generate highly complex optical states, with the scheme shown in Fig. 4(d). The scheme consists of two stages, the first stage entangles the free electron with the waveguide mode, and the second stage selects the effective measurement basis for the electron energy. Specifically, the first stage of the interaction is the same pair-state generation [46] discussed in previous sections. While direct conditioning on the electron energy measurement generates optical Fock states, in order to generate more general optical states, one can select a more general measurement basis by having a second stage to apply a unitary transformation $\hat{U}$ on the

electron state before the measurement. Starting from the physical measurement basis $\langle M|$, with the correct unitary transformation $\hat{U}$, the desired measurement basis $\langle M|\hat{U}$ can be generated. If an arbitrary measurement basis can be constructed, an arbitrary quantum state can be heralded. Such a scheme exploits the time-reversal symmetry in quantum mechanics, and has been used to demonstrate optical super-resolving phase measurement using only classical lasers [79].

In the illustrated case, shown in Fig. 4(d), we apply a standard photon-induced near-field electron-microscopy (PINEM) operation [35]

$$\hat{S}_{\mathrm{PINEM}}(g,\omega) = \exp\left(g\hat{b}_{\omega}^{\dagger} - \mathrm{h.c.}\right) \tag{11}$$

at the same optical frequency (served as the phase reference for any follow-up optical state characterization) before detection, which effectively transforms the measurement basis from $\langle E_c|$ to $\langle E_c|\hat{S}_{\mathrm{PINEM}} = \sum_N c_N \langle E_c + N\hbar\omega|$ with Bessel coefficients c_N. Upon heralding, the generated optical state is

$$|\psi_{\mathrm{ph}}\rangle \propto \sum_N \frac{c_{-(E_c/\hbar\omega+N)} g^N}{\sqrt{N!}} |N\rangle \tag{12}$$

with coefficients modified by the selected electron measurement basis. Following this scheme, if at the second stage we select a more general measurement basis by modulating the electron with an optical waveform consisting of multiple harmonics [80] of the base optical frequency $\hat{S} = \prod_n \hat{S}_{\mathrm{PINEM}}(g_n, n\omega)$, one can in principle generate any general optical state, e.g., cat and GKP state [41]. Note that in the no-recoil limit, any operation on the electron wave function commutes with the entangling operation $\hat{S}_{e\text{-ph}}$. Therefore, it does not matter if the operation is applied postentanglement or preentanglement.

Until here, we restrict ourselves to state generation in the ideal scenario where electron and photon are completely disentangled in the subspace of the synthetic electron-photon energy ladder. However, as is discussed in the theory section, there are still correlations between electron energy and optical frequency within the subspace. When tracing out the subspace continuum states, this leads to a degradation of state purity $\mathcal{P} = \mathrm{Tr}\left[\hat{\rho}^2\right]$ and fidelity $\mathcal{F} = \left|\langle\psi_{\mathrm{prepared}}|\psi_{\mathrm{target}}\rangle\right|^2$ of the synthesized quantum state $\hat{\rho}$. We analyze these effects in our state heralding scheme (expressions for $\mathcal{P}$ and $\mathcal{F}$ derived in Appendix G, calculated using Monte Carlo sampling due to high dimensionality). We first stress that when conditioning on an electron energy with perfect energy resolution, the purity of the state is always unity, and we define the state fidelity in that limit. However, the relative heralding bandwidth $\gamma = \Delta E/\Delta E_{\mathrm{ZLP}}$ determines the heralding rate, and is lower bounded by the experimental energy resolution. At finite bandwidth, it always results in finite purity of the state. We illustrate this effect at different relative heralding bandwidths in Appendix G.

We assume a ZLP width $\Delta E_{\mathrm{ZLP}} = 0.6$ eV with fitted Voigt lineshape from experimental data [46]. Given a relative heralding bandwidth $\gamma = 1$, we show in Figs. 4(e) and 4(f) both the purity $\mathcal{P}$ of the state and the fidelity $\mathcal{F}$ compared to the target state. As the purity is only a function of the occupancy at different Fock-state components, we plot only the scheme- and state-independent purity at these components. Due to more scrambled correlations between electron energy and photon frequency at higher ladder-state subspace $|\psi_e, N\rangle$, their purity is lower, with impurity $1-\mathcal{P} \propto \sqrt{N}$. We also see that fidelity and purity increase with longer interaction distance L, with $1-\mathcal{F} \propto L^{-4}$ and $1-\mathcal{P} \propto L^{-2}$. This scaling is expected from the narrower phase-matching bandwidth at longer interaction length, and aligns well with the prolonged interaction targeted by the photonic integrated circuits. To help the readers grasp the inverse quadratic scaling to interaction length, we point out that for relatively short interaction length at 10 μm [35], the state purity is $< 90\%$ for Fock-state components $|3\rangle$ and above, but for an interaction length at 100 μm [46], the state purity $> 98\%$ even for $|10\rangle$, with fidelity exceeding 99.9%.

Note that any contribution from the experimental uncertainty of electron energy will lead to degradation of the electron state purity, and also increase the relative heralding bandwidth. Therefore, the experimentally measured ZLP width approximately 0.6 eV [81] can only serve as the upper bound of the quantum coherent energy uncertainty. Experimentally, the coherent energy uncertainty can be at least lower bounded at approximately 0.1 eV by the measured single-electron pulse duration [82], which is in fact still far from the Fourier limit. In the limiting case when the electron energy density matrix is completely incoherent, $\mathcal{P} \to 0$. Furthermore, as the experimentally measured purity of the heralded optical state through Wigner tomography [83] scales as $1-\mathcal{P} \propto \Delta E_{\mathrm{coherent}}^{-2}$, the purity characterization can also serve as a probe of the coherence property of the free electron. Even though the coherent electron energy width is hard to determine experimentally, it is fundamentally determined by the electron field-emission mechanism that generates the electron pulse. We can conclude that in order to be quantum coherent, the frequency spread of the heralded optical state must be much smaller than that of the laser pulses used in the electron field emission.

IV. SHAPING ELECTRON STATES FROM OPTICAL DETECTION

Here we consider the reciprocal operation of the previous section, which is to generate complex electron energy superposition state by conditioning on photon counting.

This procedure enables generation of a much broader set of electron states not accessible by conventional PINEM-type phase modulation, e.g., direct amplitude modulation of electron wave function. Note that with the no-recoil approximation, here the heralded spatial-temporal electron wave function is not shaped by the optical detection and maintains the original waveform, in sharp contrast to heralding optical state by measuring electron energy. Therefore, the fidelity $\mathcal{F}$ of the heralded electron wave function does not depend on interaction length, but the state purity still does.

In Fig. 5(a) we illustrate a similar scheme to that shown in the previous section to generate complex electron states with multiple stages of operations but on the optical side. The principle is the same, a pair state is generated, then we select an effective measurement basis on the optical side to project the electron state into the desired form. As an example, before the detection, one can use a displacement operation $\hat{D}(\alpha)$, realized by a high-ratio on-chip beam splitter [84], to modify the effective photon number counting [85,86] measurement basis from $\langle N|$ to $\langle N|\hat{D}(\alpha) = \sum_{N'} c_{N'}\langle N'|$. Based on a photon-counting record, a conditional electron state is prepared at

$$|\psi_e\rangle \propto \int dE\psi(E)\sum_N \frac{c_N g^N}{\sqrt{N!}}|E - N\hbar\omega\rangle. \qquad (13)$$

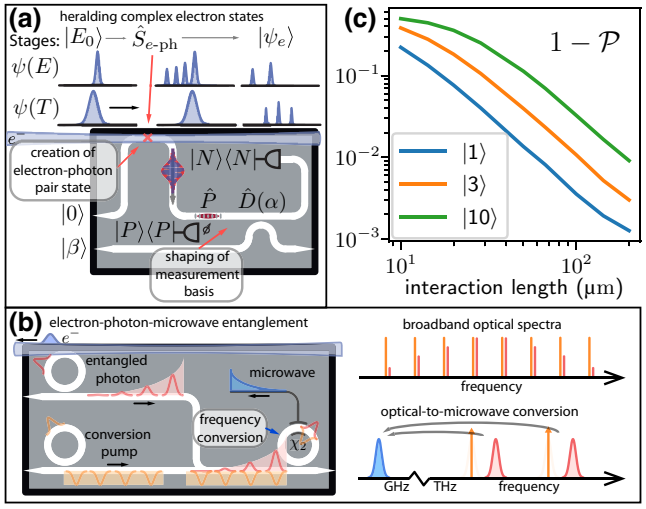

FIG. 5. (a) Scheme for heralding an arbitrary electron state by optical detection, consisting of one stage for pair-state preparation with $\hat{S}_{e\text{-ph}}$ and one stage for measurement basis selection with on-chip optical operations. (b) Scheme to convert the original THz-broad optical excitation to a MHz-broad microwave excitation, with frequency width limited by the linewidth of the optical cavity, using a χ_2 optical-to-microwave transducer. The narrow-linewidth down-converted microwave excitation is useful for interacting with GHz-frequency quantum systems at low temperatures. (c) Investigation of subspace correlation-induced degradation of purity of different electron ladder-state components $|N\rangle$ as a function of interaction length.

In the special case of the coherent-state measurement basis $\langle\alpha|$, which can also be constructed by simultaneously detecting both orthogonal optical quadratures in a homodyne setting (derivation see Appendix K), the heralding operation is equivalent to applying a direct density modulation $\exp\left(2|g\alpha^*|\cos(\frac{\omega}{v}z + \theta_\alpha)\right)$ on the electron wave function. In the limit of large modulation depth $|g\alpha^*| \gg 1$, the width of the electron wave function is compressed down to $\Delta z \sim \frac{1.7v}{\omega\sqrt{|g\alpha^*|}}$. The magnitude of pulse compression is similar to what is possible with PINEM-type interaction, but without the additional dispersive propagation with modulation-depth-dependent distance [21].

The projection into a sharply density modulated electron wave function by measuring in the basis of optical coherent states can be understood intuitively. Since classical coherent optical excitation can only be generated by pointlike electrons, the measurement of coherent states serves as a position measurement of the electrons, projecting them into the possible periodic positions that would give the correct classical phase of the measured optical coherent state. But since the coherent states are not completely orthogonal to each other, the uncertainty of the projected electron position is determined by the magnitude of the measured field amplitude $|\alpha|$.

One can also prepare even parity electron energy state to halve the spatial modulation period, useful for generating coherent second harmonic optical emission [55], by applying conditional optical parity operation $\hat{P}(P)$ using two-level systems [6,87,88] or photon-number-resolving counting [89], which modifies the measurement basis to cat states $\langle \text{cat}_\alpha| \propto \langle\alpha| + \langle -\alpha|$. Higher harmonic spatial modulation can be generated by detecting in higher-order cat-state basis.

On the optical side, most unitary operations or state characterizations require mode matching to a reference spatial-temporal optical mode, which is difficult to achieve for the emitted THz broad optical pulses. Here we discuss two options that are experimentally feasible. The first option is to reshape the emitted optical spatial-temporal profile through frequency filtering, e.g., using an on-chip photonic crystal filter cavity [6]. When the frequency width is narrow enough to be resolved by the detector, one can choose a continuous-wave local oscillator and gate on the detector time sequence [90] synchronized with the electron pulses. To prevent any loss of information that may lead to the degradation of state purity, one needs to collect all the optical excitations rejected from the filter and condition on a zero-count event from the dark port. At a single-photon level of optical emission, the relative heralding rate is determined by the filtered optical bandwidth versus the original optical phase-matching bandwidth. Therefore, such a frequency-filtering scheme does limit the heralding rate significantly due to the large phase-matching bandwidth (e.g., 1-THz width at 1-cm interaction length). The

second option is to directly mode match with a specifically shaped reference optical pulse. Such pulse shaping with individual control at all the frequency components is generally hard in straight waveguides, and therefore requires the use of optical resonators in place of waveguides as was recently demonstrated [46]. The reference optical mode can then be generated in an identical resonator [91], e.g., as a dissipative Kerr soliton [92] or an electro-optic frequency comb [93] with control over each individual frequency component [72,94]. The time gating resolution required on the optical detection would then be relaxed to the optical cavity life time, which can be achieved at the level of 20 ns [49] for materials and structures studied in the current paper. In integrated photonics, cavity life time approaching 1 μs is also demonstrated [95–97].

Optical resonators offer the unique advantage of the concentrated optical density of states due to their narrow optical linewidth. We show a frequency-conversion example in Fig. 5(b) (details of the scheme see Appendix L) to exploit this advantage of optical resonators to convert the THz-broad optical excitation from the electron-photon interaction to a MHz-broad microwave excitation using a χ_2 optical-to-microwave converter [98,99]. Using a structured local oscillator pump field, the conversion effectively serves as a multimode demodulation of the entangled photons. The frequency width of the microwave photon is determined by the linewidth of the optical cavity mediating the electron-photon interaction. Compared to the original THz-broad optical excitation, this frequency conversion is particularly useful to bridge interactions of eV-broad free electrons with quantum systems at GHz frequencies, e.g., superconducting qubits, electron-spin qubits, and mechanical oscillators. Generally, with the coupling to well-controlled two-level systems in the strong coupling regime, any photon measurement basis can be constructed [100]. As arbitrary quantum state synthesis of microwave photons was experimentally demonstrated in superconducting qubit systems [101], we can construct an arbitrary measurement basis $\langle\psi| = \langle 0|\hat{U}$ by applying the unitary operation $\hat{U}$ on the converted microwave field and then conditioning on the microwave ground state $\langle 0|$ with photon-number-resolving measurement [102] using a superconducting qubit, promising arbitrary electron-state generation. Optical-to-microwave converters and superconducting qubits mostly require mK temperatures due to their GHz frequencies, and usually operate in a dilution refrigerator. Therefore, optical excitations need to be guided out of the electron microscope through optical fibers, stressing the importance of high-efficiency fiber-to-chip couplings [50].

Note that due to multiple stages, usually the optical measurement event will occur after the electron detection due to the high electron velocity. However, a delayed measurement on the optics side does not impair our scheme, as the measurement operators on the two parties commute [103]. Therefore, no real-time action is required.

Here, we show the full-bandwidth state purity (expressions derived in Appendix H) as a function of interaction length in Fig. 5(c). As expected, it follows the same $1-\mathcal{P} \propto L^{-2}\sqrt{N}$ scaling, and favors longer interaction length. We point out again that for a relatively short interaction length at 10 μm, the electron ladder $|10\rangle$ state purity is 50%, but for an interaction length at 200 μm, the state purity reaches 99%. Note that the state purity is completely determined by the electron-photon interaction, and does not depend on specific schemes, e.g., optical-to-microwave conversion.

Here, a lower purity of the initial electron state will also result in purity degradation of the heralded electron wavefunction, similar to the case of heralded optical state discussed in the previous section. However, effects like heralded density modulation is robust as the electron position projections are always valid given optical measurement records even with mixed electron states.

V. DISCUSSION

We analyze fundamental limits of integrated photonic circuits as a platform for synthesizing high-quality quantum states with free electrons. We show that near-unity coupling ideality to the target TM_{00} spatial-temporal waveguide mode can be achieved by suppressing parasitic couplings through the control of electron-beam positioning, velocity, and waveguide design. We also investigate the underlying correlation between electron energy and photon frequency in the energy ladder subspace, and the induced fundamental limitation as a trade-off between heralding rate and state purity. We find that particlelike electrons with coherent energy uncertainty are required to generate pure heralded states, and the purity limit can be greatly relaxed with experimentally feasible interaction length with integrated waveguides. We also show that these correlations can be exploited to shape the optical waveforms, e.g., to map the electron wave function to optical domain and construct an effective optical interferometer mediated by free electrons. However, the spatial sensitivity of such an interferometer remains at the optical-wavelength scale, and does not inherit the superior spatial sensitivity of electron waves. It is still an open question whether phase-object-induced electron phases can be transferred to the optical domain, accumulate and be detected optically, which is relevant for quantum enhanced phase-object imaging applications [104,105]. The maximum feasible coupling strength $|g_{TM_{00}}|^2$ can also be further enhanced through waveguide dispersion engineering [48], with the trade-off of lower state purity due to larger phase-matching bandwidth.

Note that in our discussion we omit detailed analysis on some experimental limitations, e.g., finite detection efficiencies, primarily on the optical side. The heralded optical state is robust given the high energy of the electrons, but the heralded electron-state purity is therefore most sensitive to the optical detector efficiencies and other limiting factors, such as optical mode matching. We anticipate that there are schemes or parameter regimes that are less prone to detection inefficiencies. We also restrict our discussion mostly to the interaction picture, except that the electron and optical waveforms are defined in the Schrödinger picture. We remind the reader that in the Schrödinger picture, though not the main focus of the paper, long-distance propagation significantly modifies the electron and optical density profile $|\widetilde{\psi}(T)|^2$ and $|\phi(T)|^2$, leading to effects like electron [23,64–66,106] and optical [107] pulse compression. Moreover, in the no-recoil limit, all the electron operations commute with each other. This approximation, though practically valid for few-photon single-chip interactions, limits the controllable degrees of freedom of the heralded optical states to the order of the harmonics of the PINEM field used to shape the electron wave function [80]. In the platform of Si_3N_4 microresonators, efficient generation of second [108] and third [109,110] harmonics are supported with estimated maximum $|g_2| \sim 100$ and $|g_3| \sim 10$, offering a total of 8 degrees of freedom on the heralded optical state. The Si_3N_4 integrated photonics platform also provides an ultrawide transparency window from 400 nm to 4.5 μm [111], supporting at most ten harmonic components with an externally driven optical source. Beyond the no-recoil limit [106], electron energy transitions significantly modify the velocity due to energy dispersion. When interaction regions are far apart, the recoil effect results in an energy-dependent phase accumulation between different stages (for details see Appendix M). The recoil effect can be safely neglected in the discussion of few-photon single-chip interaction, but could be important for a wider range of experimental schemes [23,40,55,112,113], e.g., when multiple chips are involved with significant separation distance. Furthermore, our analysis is purely in the framework of macroscopic QED [68], where electrons interact with the medium-assisted electromagnetic fields. In optical media like the Si_3N_4 material we discuss here, optical phonons typically exist and result in Raman scattering of optical fields [114]. But, due to their short spatial extent and low energy [115,116], we do not consider their contribution in long-distance phase-matched interaction with the high-energy free electrons. The same reasoning also excludes higher electron energy-loss process, e.g., valence and inner-shell ionization around 50 eV [117].

Our analysis and results indicate that the photonic integrated circuit platform is ideal for free-electron quantum optics with manageable limitations, and promise a pathway to high-fidelity and high-purity quantum state heralding, entanglement of free electrons with other quantum systems, and quantum enhanced sensing and imaging.

ACKNOWLEDGMENTS

We thank Armin Feist, Germaine Arend, Thomas Juffmann, Xihang Shi, Yuval Adiv, Yujia Yang, and Terence Blésin for useful discussions. This work is supported by the Swiss National Science Foundation under Grant Agreement No. 185870 (Ambizione). O.K. gratefully acknowledges the Young Faculty Award from the National Quantum Science and Technology program of the Israeli Planning and Budgeting Committee.

APPENDIX A: QED DETAILS

We consider an electron beam with a narrow momentum spread around wave vector $\mathbf{k}_0$ and assume that the photon energies involved in the interaction are much smaller than the electron relativistic energy $E_0 = c\sqrt{c^2m^2 + \hbar^2 k_0^2}$ (i.e., the no-recoil regime). In the velocity gauge, the Hamiltonian is described as [55,118]

$$\begin{aligned}
\hat{H} &= \hat{H}_{\mathrm{el}} + \hat{H}_{\mathrm{ph}} + \hat{H}_{\mathrm{int}},\\
\hat{H}_{\mathrm{el}} &= \sum_{\mathbf{k}} [E_0 + \hbar \mathbf{v}\cdot(\mathbf{k}-\mathbf{k}_0)]\hat{c}_{\mathbf{k}}^{\dagger}\hat{c}_{\mathbf{k}},\\
\hat{H}_{\mathrm{ph}} &= \int d\omega \int d^3\mathbf{r}\hbar\omega \hat{\mathbf{f}}^{\dagger}(\mathbf{r},\omega)\cdot\hat{\mathbf{f}}(\mathbf{r},\omega),\\
\hat{H}_{\mathrm{int}} &= -\int d^3\mathbf{r}\hat{\mathbf{J}}(\mathbf{r})\cdot\hat{\mathbf{A}}(\mathbf{r}),
\end{aligned}$$

where we define the electron current operator $\hat{\mathbf{J}}(\mathbf{r}) = (-e\mathbf{v}/V)\sum_{\mathbf{k},\mathbf{q}} e^{i\mathbf{q}\cdot\mathbf{r}}\hat{c}_{\mathbf{k}}^{\dagger}\hat{c}_{\mathbf{k}+\mathbf{q}}$ using the Fermionic ladder operators $\hat{c}_{\mathbf{k}}$ and the relativistic electron group velocity $\mathbf{v} = \hbar c^2\mathbf{k}_0/E_0$, and a linear electron energy dispersion is assumed. The vector potential $\hat{\mathbf{A}}(\mathbf{r},t) = \int \frac{d\omega}{2\pi}\hat{\mathbf{A}}(\mathbf{r},\omega)e^{i\omega t} + \mathrm{h.c.}$ is associated with the noise current operator $\hat{\mathbf{j}}^{\mathrm{noise}}(\mathbf{r},\omega)$ through the quantized three-dimensional Maxwell equation [68] and has a formal solution

$$\hat{\mathbf{A}}(\mathbf{r},\omega) = -4\pi\int d^3\mathbf{r}' G(\mathbf{r},\mathbf{r}',\omega)\cdot\hat{\mathbf{j}}^{\mathrm{noise}}(\mathbf{r}',\omega),$$

where $G(\mathbf{r},\mathbf{r}',\omega)$ is the dyadic Green function (Green tensor) of the classical problem satisfying the equation

$$\begin{aligned}
&\nabla\times\nabla\times G(\mathbf{r},\mathbf{r}',\omega) - \frac{\omega^2}{c^2}\epsilon(\mathbf{r},\omega)G(\mathbf{r},\mathbf{r}',\omega)\\
&\quad = -\mu_0\delta(\mathbf{r}-\mathbf{r}'),
\end{aligned}$$

which describes the field response at $\mathbf{r}$ to a point current excitation at $\mathbf{r}'$. Since we are dealing with nonmagnetic

materials, we assume a relative permeability $\mu(\mathbf{r}) = 1$. The noise operator is bosonic and is chosen to be

$$\hat{\mathbf{j}}^{\text{noise}}(\mathbf{r},\omega) = \omega\sqrt{\hbar\epsilon_0 \text{Im}\{\epsilon(\mathbf{r},\omega)\}}\hat{\mathbf{f}}(\mathbf{r},\omega)$$

in order to satisfy the fluctuation-dissipation theorem due to dissipative material, with bosonic ladder operators $\hat{\mathbf{f}}(\mathbf{r},\omega)$ satisfying commutation relation $\left[\hat{f}_i(\mathbf{r},\omega),\hat{f}_{i'}(\mathbf{r}',\omega')\right] = \delta_{i,i'}\delta(\mathbf{r}-\mathbf{r}')\delta(\omega-\omega')$. Note that in the limiting case of a dispersive material (assumed in this study, characterized by its instantaneous electronic response) $\text{Im}\{\epsilon(\mathbf{r},\omega)\} \to 0$. However, this imposes no problem for our formalism, which is shown to correctly reduce to the mode decomposition method used in the quantized vacuum field [119] due to Kramers-Kronig relations.

When projecting to the direction of the electron trajectory $\hat{\mathbf{z}}$ with transverse coordinate $\mathbf{R}_0$, the scattering matrix is shown to be

$$\hat{S} = e^{i\hat{\chi}}\hat{U},$$

$$\hat{U} = \exp\left\{\left[\frac{-ie}{2\pi\hbar V^{2/3}}\sum_{\mathbf{k},\mathbf{q}_\perp}\int d\omega\int d^3\mathbf{r}e^{i\mathbf{q}_\perp\cdot\mathbf{R}}e^{-i\omega z/v_e}\right.\right.$$
$$\left.\left.\hat{A}_z(\mathbf{r},\omega)\hat{c}^\dagger_{\mathbf{k}}\hat{c}_{\mathbf{k}+\mathbf{q}_\perp-(\omega/v)\hat{\mathbf{z}}}\right] - \text{h.c.}\right\},$$

where $\mathbf{q}_\perp$ is the transverse component of the exchanged electron wave vector. We can further simplify the expression by disregarding the phase operator $\hat{\chi}$ and assuming a point electron distribution over the transverse direction, and obtain

$$\hat{U} = \exp\left[\int d\omega g_\omega \hat{b}^\dagger_\omega \hat{a}_\omega - \text{h.c.}\right],$$

where continuum photon and electron operators are introduced

$$\hat{a}_\omega = -\frac{ie}{2\pi\hbar g_\omega}\int dz e^{-i\omega z/v_e}\hat{A}_z(\mathbf{R}_0,z,\omega),$$
$$\hat{b}_\omega = \sum_{k_z}\hat{c}^\dagger_{k_z}\hat{c}_{k_z+\omega/v},$$

with vacuum coupling strength g_ω associated with the EELS probability studied in this paper

$$|g_\omega|^2 = \Gamma(\mathbf{R}_0,\omega) = \frac{4e^2}{\hbar}\iint dzdz',$$
$$\text{Re}\{ie^{i\omega(z-z')/v}G_{zz}(\mathbf{R}_0,z;\mathbf{R}_0,z';\omega)\}.$$

The operators are defined in this way so that the quantum optical commutation relations are preserved $[\hat{a}_\omega,\hat{a}^\dagger_{\omega'}] = \delta(\omega-\omega')$, and can be easily proven using the identity

$$\sum_{i''}\int d^3\mathbf{r}''\text{Im}\{\epsilon(\mathbf{r}'',\omega)\}G_{i,i''}(\mathbf{r},\mathbf{r}'',\omega)G^*_{i',i''}(\mathbf{r}',\mathbf{r}'',\omega)$$
$$= -\frac{1}{\epsilon_0\omega^2}\text{Im}\{G_{i,i'}(\mathbf{r},\mathbf{r}',\omega)\}.$$

Note that $\hat{a}_\omega$ contains contributions from all the spatial modes at ω, and is not a specific predefined spatial mode $\hat{a}_{\omega,m}$, which is frequently used in cavity QED systems.

To find the spatial mode function of $\hat{a}_\omega$, we use the following relations [120] for an arbitrary set of orthogonal basis $\hat{a}_{i,\omega}$

$$\hat{a}_{i,\omega} = \int d^3\mathbf{r}\mathbf{V}_i(\mathbf{r},\omega)\cdot\hat{\mathbf{f}}(\mathbf{r},\omega),$$
$$\hat{\mathbf{f}}(\mathbf{r},\omega) = \sum_i \mathbf{V}^\dagger_i(\mathbf{r},\omega)\hat{a}_{i,\omega},$$

where the weight functions obeys the following normalization condition:

$$\int d^3\mathbf{r}\mathbf{V}_i(\mathbf{r},\omega)\cdot\mathbf{V}^\dagger_j(\mathbf{r},\omega) = \delta_{i,j}.$$

From here, we can re-express the field operator in terms of the set of orthogonal basis as

$$\hat{\mathbf{A}}(\mathbf{r},\omega) = -4\pi\omega\int d^3\mathbf{r}'\sqrt{\hbar\epsilon_0\text{Im}\{\epsilon(\mathbf{r}',\omega)\}}G(\mathbf{r},\mathbf{r}',\omega)$$
$$\cdot\sum_i\mathbf{V}^\dagger_i(\mathbf{r}',\omega)\hat{a}_{i,\omega}.$$

By choosing one of the spatial modes $\hat{a}_{i=0,\omega}$ as our mode of interest $\hat{a}_\omega$ with the weight function

$$\mathbf{V}_{\hat{a}_\omega}(\mathbf{r},\omega) = -\frac{2ie\omega}{g_\omega}\sqrt{\frac{\epsilon_0}{\hbar}}\int dz e^{-i\omega z/v_e}$$
$$\int d^3\mathbf{r}'\sqrt{\text{Im}\{\epsilon(\mathbf{r}',\omega)\}}\hat{\mathbf{z}}\cdot G(\mathbf{R}_0,z;\mathbf{r}';\omega),$$

we can find the mode function of this optical mode as

$$\hat{\mathbf{A}}_{\hat{a}_\omega}(\mathbf{r},\omega) = 2\pi\sqrt{\frac{\hbar}{2\omega\epsilon_0}}\mathbf{U}_{\hat{a}_\omega}(\mathbf{r},\omega)\hat{a}_\omega,$$

$$\mathbf{U}_{\hat{a}_\omega}(\mathbf{r}) = \frac{-4e}{g^*_\omega}\sqrt{\frac{2\epsilon_0\omega}{\hbar}}\int dz e^{i\omega z/v_e}\text{Im}[G(\mathbf{r};\mathbf{R}_0,z;\omega)\cdot\hat{\mathbf{z}}],$$

which is a mode specifically defined for this interaction. This mode construction corresponds to a linear transformation of the original structure-supported optical spatial modes, such that only one principle optical mode is

involved in the interaction, while all the other transformed modes are dark and invisible to the electron. It is in this way advantageous to use this formalism to account for the infinite number of spatial modes of the optical structure that the electron couples to. In the limit of unity coupling ideality, this mode function converges to the one of the waveguide modes. If the electron transverse spread is significant, the EELS probability is shown [121] to be an average over the transverse electron wave function

$$\Gamma(\omega) = \int d^2\mathbf{R}|\psi_\perp(\mathbf{R})|^2\Gamma(\mathbf{R},\omega).$$

However, this type of averaging is not quantum coherent. At different transverse positions, the coupling coefficients are different. Therefore, we have to modify the scattering matrix to

$$\hat{S} = \exp\left[\int d\omega d^2\mathbf{R} g_\omega(\mathbf{R})\hat{b}^\dagger_\omega|\mathbf{R}\rangle\langle\mathbf{R}|\hat{a}_\omega - \text{h.c.}\right].$$

If the part of the longitudinal optical field that overlaps with the electron transverse wave function has considerable inhomogeneity, then the different transverse position components of the electron will be entangled with different longitudinal electron-photon pair states, characterized by their different coupling strengths. Therefore, information loss occurs when tracing out the transverse degrees of freedom of the electron, leading to state purity degradation. Since nm-scale electron beam focuses are routinely used in electron microscopes, this is not a significant limitation for near-field coupling to optical waveguides which have a typical decay length of approximately 100 nm.

APPENDIX B: EQUIVALENCE TO THE CLASSICAL RESULT

The electron energy loss at a dielectric surface can be interpreted classically in a microscopic picture [122], see Fig. 1: if an electron passes near the surface of a dielectric structure, the dipoles in the structures are polarized (equivalently classical current), induced by the electric field from the flying electron, and generates a backaction field $\mathbf{E}(\mathbf{r}_e(t),t)$ to the electron at $\mathbf{r}_e(t)$ that induces electron energy loss. The total energy loss can be expressed in time domain and frequency domain as

$$\Delta E = e\int dt\mathbf{v}\cdot\mathbf{E}(\mathbf{r}_e(t),t) = \int \hbar\omega d\omega\Gamma(\omega),$$

where the frequency-domain energy-loss function $\Gamma(\omega)$ is expressed as

$$\Gamma(\omega) = \frac{e}{\pi\hbar\omega}\int dt\text{Re}\left[e^{-i\omega t}\mathbf{v}\cdot\mathbf{E}(\mathbf{r}_e(t),\omega)\right],$$

which can be easily verified if one plugs it back into the energy-loss expression and the correct time integral is retrieved. Notice that here $\mathbf{E}(\mathbf{r}_e(t),\omega)$ is not the direct Fourier transform of $\mathbf{E}(\mathbf{r}_e(t),t)$. The Fourier transform applies only on the time dependence of the electric field function not explicitly depending on the electron trajectory function $\mathbf{r}_e(t)$. The frequency-domain components depend explicitly on the current induced from a given electron trajectory, but do not take into account the sampling of the field at different position $\mathbf{r}_e(t)$ at different time t. This ensures that the total energy loss is consistent, but renders the formalism nonlocal. This treatment is consistent with the quantum formalism when the electron is decomposed into perfect momentum states where the wavepacket length is infinite, as one could see from the fact that even though the electron interacts only with the structure locally, the resulting energy-loss spectrum will show, e.g., discrete mode structure (a nonlocal property). This is the result of this particular Fourier-expansion procedure, but when considering the electron in terms of wavepackets this treatment is valid. It has been shown [121] that a full quantum treatment gives exactly the same EELS result.

Using the no-recoil approximation, which assumes that the radiation of electron into the surrounding substrates does not change the trajectory $\mathbf{r}_e(t)$ of the electron significantly, we can directly calculate the induced electric field $\mathbf{E}(\mathbf{r}_e(t),t)$ from the electron current $\mathbf{j}(\mathbf{r},t)$ through the Green tensor of the whole dielectric structure,

$$\mathbf{E}(\mathbf{r},\omega) = -4\pi i\omega\int d^3\mathbf{r}' G(\mathbf{r},\mathbf{r}',\omega)\cdot\mathbf{j}(\mathbf{r}',\omega),$$

where the Green tensor $G(\mathbf{r},\mathbf{r}',\omega)$ is the elementary solution of the full Maxwell equation

$$\nabla\times\nabla\times G(\mathbf{r},\mathbf{r}',\omega) - \frac{\omega^2}{c^2}\epsilon(\mathbf{r},\omega)G(\mathbf{r},\mathbf{r}',\omega) = -\mu_0\delta(\mathbf{r}-\mathbf{r}')$$

with a point current at position $\mathbf{r}'$ in frequency domain. A flying electron is equivalent to a broadband evanescent source, and here we consider an electron beam at $\hat{\mathbf{z}}$ direction at transverse coordinate $\mathbf{R}_0$, for which the frequency-domain electron current density is

$$\mathbf{j}(\mathbf{r},\omega) = -e\hat{\mathbf{z}}\delta(\mathbf{R}-\mathbf{R}_0)e^{i\omega(z-z_0)/v}.$$

From here, one can express the frequency-domain loss rate in terms of Green function as

$$\Gamma(\omega) = \frac{4e^2}{\hbar}\int dzdz'\text{Re}\left[ie^{i\frac{\omega(z-z')}{v}}G_{zz}(\mathbf{R}_0,z;\mathbf{R}_0,z';\omega)\right],$$

which coincides with the result from a full QED treatment. One should keep in mind that the Green tensor here has two contributions, one from vacuum G_0 when there is no structure around, and the other component from the

backaction field G_{ind} that is induced from the dielectric dipoles. Only the backaction field G_{ind} contributes to electron energy loss, because electron does not emit in vacuum so the contribution from the vacuum G_0 vanishes in the integral.

APPENDIX C: CORRESPONDENCE TO MODAL DECOMPOSITION

The correspondence between the three-dimensional macroscopic quantization method in a dispersive material with the conventional quantum optics quantization procedure using modal decomposition has been demonstrated for the one-dimensional case [119]. Here, we show the correspondence with the quantum optical formalism used in Ref. [35]. To account for all the spatial modes at a given frequency ω, the quantization of vector potential is chosen as

$$\hat{\mathbf{A}}(\mathbf{r},\omega) = -4\pi\omega \int d^3\mathbf{r}' \sqrt{\hbar\epsilon_0 \mathrm{Im}\{\epsilon(\mathbf{r}',\omega)\}} G(\mathbf{r},\mathbf{r}',\omega) \cdot \hat{\mathbf{f}}(\mathbf{r}',\omega)$$

to fulfill the canonical field commutation relations. However, in vacuum or lossless media, the modal decomposition method [123] is often used instead, with

$$\hat{\mathbf{A}}(\mathbf{r},t) = \sum_m \sqrt{\frac{\hbar}{2\omega_m\epsilon_0}} \mathbf{U}_m(\mathbf{r}) \hat{a}_{\omega_m,m} e^{-i\omega_m t} + \mathrm{h.c.},$$

where the profile function $\mathbf{U}_m(\mathbf{r})$ of each mode defined in a frequency window $\Delta\omega_m$ satisfies the wave equation

$$\nabla \times \nabla \times \mathbf{U}_m(\mathbf{r}) - \frac{\omega^2}{c^2}\epsilon(\mathbf{r},\omega_m)\mathbf{U}_m(\mathbf{r}) = 0,$$

with normalization condition

$$\int d^3\mathbf{r}\epsilon(\mathbf{r},\omega_m)\mathbf{U}_m(\mathbf{r}) \cdot \mathbf{U}_n^*(\mathbf{r}) = \delta_{m,n}.$$

From here, one can easily find the correspondence between the spatial mode ladder operators $\hat{a}_{\omega,m}$ and the bosonic ladder operators $\hat{\mathbf{f}}(\mathbf{r}',\omega)$ as

$$\hat{a}_{\omega_m,m} = -4\pi \int_{\Delta\omega_m} d\omega \iint d^3\mathbf{r} d^3\mathbf{r}' \times \sqrt{2\omega^2\omega_m \mathrm{Im}\{\epsilon(\mathbf{r}',\omega)\}\epsilon_0}\epsilon(\mathbf{r},\omega)\mathbf{U}_m^*(\mathbf{r}) \cdot G(\mathbf{r},\mathbf{r}',\omega) \cdot \hat{\mathbf{f}}(\mathbf{r}',\omega),$$

with their vacuum coupling strength to the electron as [46]

$$g_{\omega_m,m}(\mathbf{R}_0) = -i\sqrt{\frac{e^2}{2\epsilon_0\hbar\omega_m}} \int dz e^{-i\omega_m z/v_e} U_{m,z}(\mathbf{R}_0,z).$$

In this formalism, we can rewrite the scattering matrix in its modal decomposition form

$$\hat{S} = e^{i\hat{\chi}} \exp\left[\int d\omega g_\omega \hat{b}_\omega^\dagger \hat{a}_\omega - \mathrm{h.c.}\right] = e^{i\hat{\chi}'} \exp\left[\sum_m g_{\omega_m,m}\hat{b}_{\omega_m}^\dagger \hat{a}_{\omega_m,m} - \mathrm{h.c.}\right],$$

where the optical mode operators $\hat{a}_{\omega_m,m}$ are no longer continuum mode operators and now satisfy $[\hat{a}_{\omega_m,m}, \hat{a}_{\omega_n,n}^\dagger] = \delta_{m,n}$.

In the case of an optical cavity, the optical modes are well-defined bosonic modes. As long as the electron energy resolution does not resolve frequency components of the optical mode, the treatment is valid. For an open waveguide, the modes that are coupled to the electron are instead traveling modes in a continuum [124]. This is the most general case and can include the open cavity modes as well. The vacuum coupling strength of a continuum frequency mode in a spatial mode family is

$$g_{\omega,m}(\mathbf{R}_0) = -i\sqrt{\frac{e^2}{2\epsilon_0\hbar\omega}} \int dz e^{-i\omega z/v_e} \tilde{U}_{m,z}(\mathbf{R}_0,z,\omega),$$

where the profile function $\tilde{\mathbf{U}}_m(\mathbf{r},\omega)$ satisfies the wave equation as well, but with normalization condition

$$\int d^3\mathbf{r}\epsilon(\mathbf{r},\omega)\tilde{\mathbf{U}}_m(\mathbf{r},\omega) \cdot \tilde{\mathbf{U}}_n^*(\mathbf{r},\omega') = \delta_{m,n}\delta(\omega,\omega').$$

Index m here represents different spatial mode families. However, when the electron energy resolution does not resolve the frequency structure of the coupling strength to any given mode family, as in the *weak correlation regime* discussed in the paper, one can still define the corresponding noncontinuous operators for different mode families,

$$\hat{a}_m = \int d\omega \phi_m^*(\omega)\hat{a}_\omega,$$
$$\hat{a}_\omega = \sum_m \phi_m(\omega)\hat{a}_m,$$

where $\phi_m(\omega)$ is the Fourier component of the temporal field profile functions [125,126]

$$\phi_m(\mathbf{r},t) = i\int d\omega \sqrt{\frac{\hbar\omega}{2\epsilon_0}}\phi_m(\omega)\tilde{\mathbf{U}}_m(\mathbf{r},\omega)e^{-i\omega t},$$
$$\hat{E}(\mathbf{r},t) = \sum_m \phi_m(\mathbf{r},t)\hat{a}_m + \mathrm{h.c.}$$

of the defined mode families. It is a complete orthogonal set of functions on ω,

$$\int d\omega \phi_m(\omega)\phi_n^*(\omega) = \delta_{m,n},$$
$$\sum_m \phi_m(\omega)\phi_m^*(\omega') = \delta(\omega - \omega')$$

found through the Gramm-Schmit orthonormalization procedure, such that the commutation relation $[\hat{a}_m, \hat{a}_n^\dagger] = \delta_{m,n}$ is satisfied for these *field operators* in the context of quantum field theory, introduced to avoid using operator-valued distributions. One can therefore rewrite the scattering matrix in the new mode family field operator basis

$$\hat{S} = e^{i\hat{\chi}} \exp\left[\sum_m g_m \hat{b}_m^\dagger \hat{a}_m - \text{h.c.}\right],$$

where $g_m = \int d\omega g_\omega \phi_m(\omega)$. The total coupling strength would be $|g_m|^2 = \iint d\omega d\omega' g_\omega g_{\omega'}^* \phi_m(\omega)\phi_m^*(\omega')$. Here, when the frequency bands of different mode families with non-negligible coupling strength g_ω are sufficiently separated, we choose the profile function $\phi_m(\omega) = \mathbb{I}_{\omega\in\Delta\omega_m} g_\omega^*/g_m^*$, where $\Delta\omega_m$ is the frequency window within which we define the field operator for the corresponding mode family, and $|g_m|^2 = \int_{\Delta\omega_m} d\omega |g_\omega|^2$. Note that when the coupling to bulk modes is significant, one has to use the coupling strength $g_{\omega,m}$ from the conventional modal decomposition method instead of the Green function method to quantitatively isolate the coupling to a mode family from background bulk mode contributions.

The cavity-mode decomposition is actually the narrowband approximation of the Gramm-Schmit orthonormalization procedure, where $\phi_m(\omega)$ is strongly peaked around the mode center frequency, since all optical modes, though narrow, still have a finite linewidth due to the coupling to outside channels (e.g., bus waveguide and cavity losses). The profile function can be found through the input-output formalism [127] of an optical cavity $\hat{a}_m$, assuming unity coupling efficiency to the bus waveguide mode $\hat{a}_{\text{out}}$ with coupling rate κ, which results in a profile function of $\phi_m(\omega) \propto \frac{\sqrt{\kappa}}{-\frac{\kappa}{2}+i(\omega_m-\omega)}$, where the bus waveguide is part of the resonator and forms the continuum modes in frequency domain.

APPENDIX D: COMSOL SIMULATION DETAILS

Since all the physical quantities we are interested in can be related to the Green tensor of the classical Maxwell equation given the dielectric structure of interest, we numerically solve the relevant Green tensor component $G_{zz}(\mathbf{r}, \mathbf{r}', \omega)$ of an infinitely long optical waveguide with finite-element method (FEM). The spatial map of the imaginary part of the Green function is illustrated in Fig. 6. The Green function can be understood intuitively as the Fourier component of the optical field at frequency ω that is excited at position $\mathbf{r}$ by the propagating electron at position $\mathbf{r}'$, whereas the phase-matching condition determines whether this field constructively or destructively builds up at a given electron velocity.

The Green tensor solution of Maxwell equation is not directly supported in COMSOL, but can be retrieved by frequency-domain study with the rf module. The waveguide is an air-cladded Si_3N_4 slab embedded in SiO_2 substrate with different geometries mentioned in the main text. Perfect matching layers at boundaries are used to prevent boundary reflections and in turn allow us to simulate an infinitely long waveguide. In order to solve for

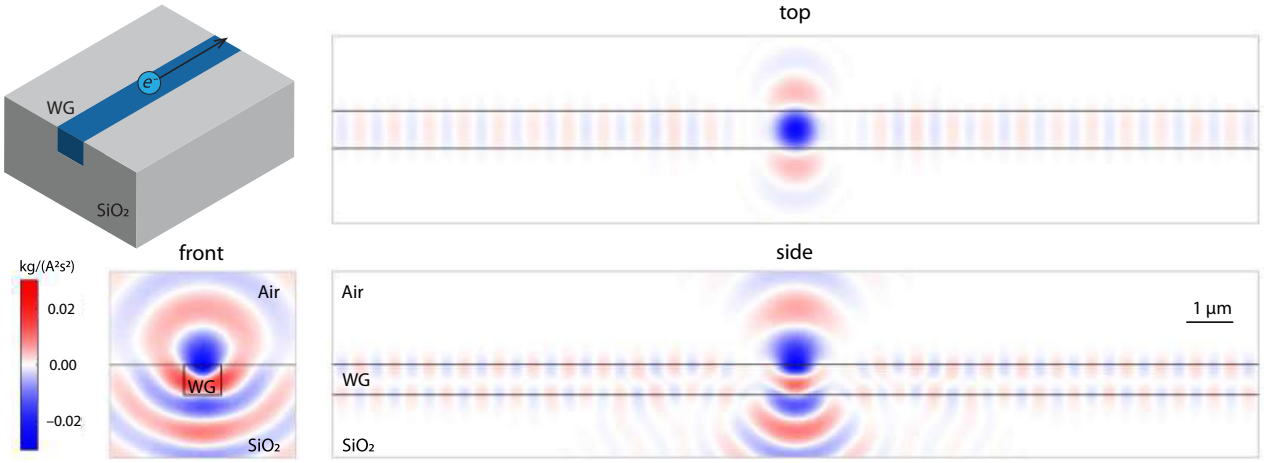

FIG. 6. Spatial pattern of $\text{Im}[G_{zz}(\mathbf{r}, \mathbf{r}_0, \omega)]$ for the case of a Si_3N_4 waveguide embedded in a silica substrate. In addition to emission into the substrate and free space, some guided modes in the waveguide are also excited by the oscillating electric current dipole, and forms a beating spatial pattern amongst guided modes along the waveguide direction.

the Green function $G(\mathbf{r}, \mathbf{r}', \omega)$, a point oscillating electric current dipole $\mathbf{J}(\omega) = \mathbf{p}(\omega)\delta(\mathbf{r} - \mathbf{r}_0)$ is placed above the waveguide surface at position $\mathbf{r}_0$ (typically 100 nm or 300 nm). COMSOL solves for the electric field, which relates to the Green tensor as

$$\mathbf{E}(\mathbf{r}, \omega) = -4\pi i\omega G(\mathbf{r}, \mathbf{r}_0, \omega) \cdot \mathbf{p}(\omega)$$

and thus if one wishes to retrieve the G_{zz} component one needs to orient the electric dipole $\mathbf{p} = p\hat{\mathbf{z}}$ along the z direction $\hat{\mathbf{z}}$, and look at the electric field z component E_z, such that

$$G_{zz}(\mathbf{r}, \mathbf{r}', \omega) = \frac{E_z(\mathbf{r}, \omega)}{-4\pi i\omega p(\mathbf{r}', \omega)}.$$

The results are illustrated in Fig. 6. The imaginary part of the Green function can be thought of as the spatial pattern of electron emission in the waveguide (or surrounding substrates) before the application of phase-matching condition. Given the electron velocity, the application of phase matching

$$\mathbf{U}_{\hat{a}_\omega}(\mathbf{r}) \propto \int dz e^{i\omega z/v_e} \mathrm{Im}[G(\mathbf{r}; \mathbf{R}_0, z; \omega) \cdot \hat{\mathbf{z}}],$$

retrieves the field function of the excited optical mode. The Green function along the electron trajectory is shown in Fig. 7(a), where one can clearly see the bulk mode contribution near the dipole position, and spatial beatings of different waveguide modes under some conditions.

With the optimal phase-matching condition, the coupling strength at a given optical frequency (or a discrete cavity mode) scales quadratically with the interaction length, a unique feature of guided modes co-propagating with the flying electron. For the spatial modes in the substrate bulk, the excited field is localized around the electron position. Without the benefit of constructive interference from co-propagation with the flying electron, their intensity only scales linearly with respect to interaction length.

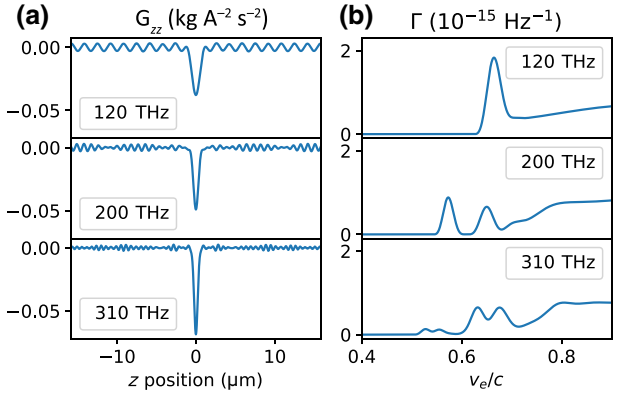

FIG. 7. (a) Examples of the Green function $\mathrm{Im}[G_{zz}(\mathbf{r}, \mathbf{r}_0, \omega)]$ along the trajectory of the electron at different optical frequencies, and (b) the corresponding vacuum coupling strength at different electron velocities, for a 50-μm interaction length. The spatial beating of many mode families is visible in the Green functions, and also in the coupling strength. The coupling to different mode families is phase matched at different electron velocities at a given optical frequency. When the electron velocity is in the Cherenkov regime ($v \gtrsim 0.7c$), the energy loss is eventually dominated by the substrate loss.

The total coupling strength is related to the Green function through a spatial Fourier transform, and shown in Fig. 7(b), where one can identify several prominent peaks, mainly contributed from the waveguide modes, and a rising background in the Cherenkov regime ($v \gtrsim 0.7c$) of the silica substrate due to the enhanced bulk mode coupling. The Blackman window is used to eliminate the ripples from the Fourier transform due to finite simulation length, and shapes each coupling bands to a near-Gaussian shape for easier fitting of the coupling strength with a Gaussian function. The center velocity of the peaks corresponds to the optical mode phase velocity, and the bandwidth is determined by the interaction length. To improve visualization, we set the interaction length to 30 wavelengths to keep the bandwidths at different optical frequencies uniform. By sweeping the optical frequency in the simulation across the range where we have access to material permittivity, one retrieves the two-dimensional maps shown in Fig. 8.

With a multimode waveguide, shown in Figs. 8(a) and 8(b), the effective mode index difference between the fundamental mode and higher-order modes is relatively weak at the same optical frequency, which leads to multimode electron-photon interaction within a given frequency band. When the waveguide cross section is reduced (referred to as *single-mode* waveguide), shown in Fig. 8(c), one can enhance the mode index contrast. As a result, the mode frequency spacing is increased, such that the coupled fundamental modes are better isolated. Since most TEMs have an energy resolution around 0.5 eV (120 THz in optical frequency), it is important to create a large frequency spacing between the phase-matched optical modes so that the interaction with individual modes can be energy resolved.

The difference between multimode and single-mode waveguides in fiber optics is usually quantified by a V number, a normalized frequency parameter, which determines the number of modes of a step-index fiber, as

$$V = \frac{2\pi r}{\lambda}\sqrt{n_1^2 - n_2^2},$$

where r is the radial size of the core, n_1 is the core material index and n_2 is the cladding material index. For our single-mode waveguide dimension, the single-mode guiding criteria $V < 2.4$ is satisfied. When used in the

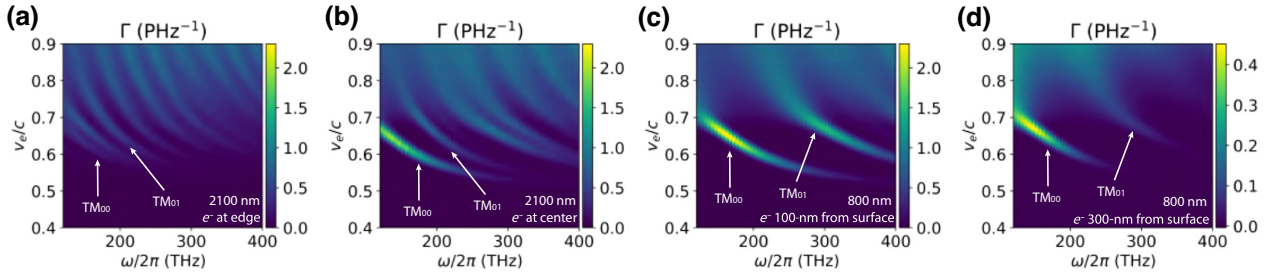

FIG. 8. Electron-photon coupling spectrum with 50-μm interaction length for different waveguide geometries and electron positioning. The coupling spectrum is plotted as a function of both electron velocity v_e and optical frequency ω. The waveguides have a thickness of 650 nm, and widths of (a),(b) 2.1 μm and (c),(d) 800 nm, and are embedded in a silica substrate. Coupling to different waveguide mode families appears as multiple coupling bands. Coupling ideality to the target TM_{00} mode is improved by changing the electron-beam transverse position from waveguide edge (100 nm from surface) (a) to waveguide center (b), from multimode waveguide (b) to single-mode waveguide (c), and moving further away (300 nm from the surface) (d) from the waveguide surface. The waveguide widths and the relative positions of the electron beam are also labeled at the lower right corner of the panels.

fiber-optic applications, such a criterion is very important for single-mode guiding. Here, our design goal is to increase the mode-frequency spacing between mode families. Therefore, we use it only as a guiding principle, not as a strict criterion.

The evanescent field of the coupled higher-order modes decay faster than that of the coupled fundamental mode, as a result of the higher optical frequency. In Fig. 8(d), we show that one can further enhance the coupling contrast between fundamental mode and higher-order modes by placing the electron beam further away (200 nm) from the waveguide surface. In this way, the interaction exponentially favors the fundamental mode, at the expense of weaker interaction strength $|g_{TM_{00}}|^2$, which can be compensated for with a longer interaction length (5 times longer for the shown example).

As discussed in the main text, the Cherenkov radiation contributes as a rising background in the high velocity region. In Appendix E, we isolate the contribution of the substrate bulk modes.

We now quantitatively evaluate the coupling ideality to the TM_{00} mode as a function of electron velocity. We fit the coupling spectra with Gaussian functions, illustrated in Fig. 9(a), and calculate the conditional and nonconditional idealities as a function of electron velocities, shown in Figs. 9(b) and 9(c).

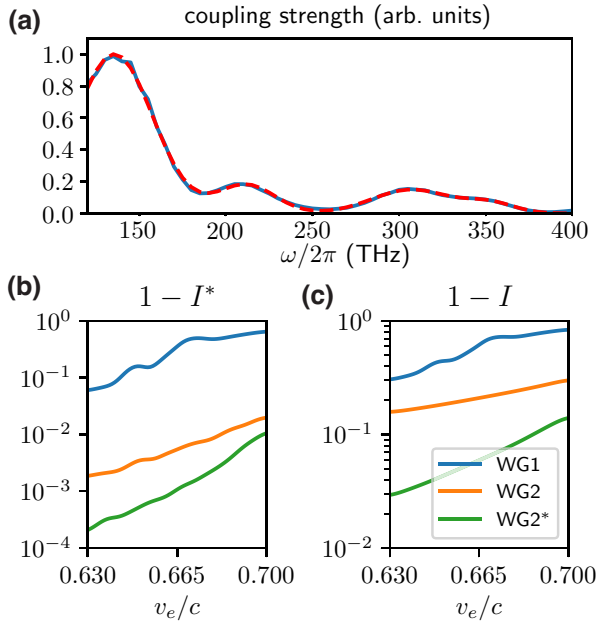

FIG. 9. (a) An example fitting of the coupling spectrum to extract the coupling idealities. Calculated coupling ideality deviations from unity with (b) sideband-conditioned ($1 - I^*$) and (c) nonconditional ($1 - I$), shown with different waveguide and electron configurations (WG1, 2.1 μm width; WG2, 800 nm width; WG2*, electron beam 200 nm further away from the waveguide surface), as a function of electron velocity.

APPENDIX E: SUBSTRATE AND THIN-FILM LOSSES

Though not discussed in the main text, there are different scalings of $\Gamma(\omega)$ for bulk substrate ($\propto L$), thin film ($\propto L \log L$), and guided modes ($\propto L^2$). We show their coupling spectrum characteristics in Fig. 10 with an electron 100 nm above the dielectric surface. It is shown that for a given frequency component ω, the quadratic scaling of a guided mode will dominate the interaction. However, for a waveguide structure with linear dispersion [e.g., the one shown in Fig. 10(a)], the phase-matching condition will enforce a linear scaling of the total deposited quanta into one particular waveguide mode. But due to relatively weak dispersion of the waveguide modes, the coupling contribution from the waveguide modes dominates over substrate losses, where the latter accounts for far less than 1% of the total coupling strength over a 0.6-eV band with electron velocity $v_e/c \leq 0.6$. For unpatterned thin films, the total photon emission is 70% lower than for a waveguide, and

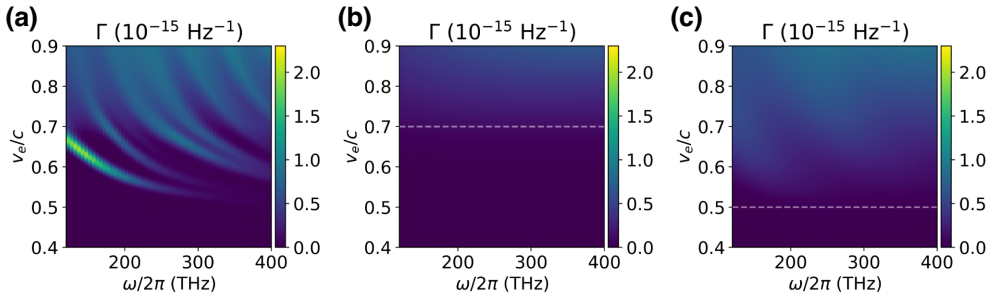

FIG. 10. Electron energy-loss spectrum for a 50-μm interaction distance with (a) waveguides, (b) silica substrate, and (c) Si_3N_4 thin film on silica substrate. Notice that for a waveguide the scaling is quadratic with respect to distance and more structured, whereas for substrate and thin film the scaling is mostly linear and the emission is more broadband. The interaction with the waveguide mode will prevail over substrate and thin film over an interaction length of just a few wavelengths. The dashed gray lines are a guide to the eye showing Cherenkov regime boundaries for silica and Si_3N_4.

the emission is less structured and hard to collect. Note that due to the presence of chromatic dispersion, the total coupling strengths of different spatial-temporal optical modes are linearly dependent on distance. Therefore, the ratio of different coupling contributions is distance independent, and depends only on waveguide dispersion and routing, and *e*-beam positioning.

APPENDIX F: INTERACTION WITH OPTICAL RESONATORS

We discussed only results for open-ended waveguides so far. However, there have been experiments [35,46] that use optical resonators with a discrete set of well-defined frequency modes instead of a continuum of frequency modes in the case of a waveguide. These well-defined modes in state-of-the-art resonators typically have optical linewidths of tens of MHz [49], and it is therefore difficult to resolve their Green functions by sweeping the optical frequencies in FEM simulations. Nonetheless, their Green functions can be easily related to the one of the open-ended optical waveguides by their optical susceptibility function $\chi(\omega) = \frac{2}{\pi}\frac{F}{1+4(\omega-\omega_0)^2/\kappa^2}$ enforced by the resonator periodic boundary conditions, describing an optical resonance with center frequency ω and Finesse $F = \frac{\Delta\nu_{\mathrm{FSR}}}{\kappa}$, where the cavity free-spectral-range (FSR) is used. One can retrieve the resonator Green function $G(\omega)$ by separating the open waveguide Green function into contributions from different cavity modes [with mode field function $\mathbf{U}_m(\mathbf{r})$, details see Appendix C]

$$G_m(\mathbf{r},\mathbf{r}',\omega) = \mathbf{U}_m(\mathbf{r}')\int d^3\mathbf{r}''\epsilon(\mathbf{r}'',\omega)\mathbf{U}_m^*(\mathbf{r}'')G(\mathbf{r},\mathbf{r}'',\omega),$$

and multiplying the resonance susceptibilities $G(\omega) = \sum_m G_m(\omega)\chi_m(\omega)$. For a closed-loop resonator structure, the resulting interaction strength $\Gamma(\omega)$ will have a narrow-linewidth comblike structure [46] instead in frequency space, compared to the continuum case of an open-ended waveguide, with the peak intensity enhanced by a factor of $\frac{2F}{\pi}$.

A comparison between a waveguide and a resonator coupling to free electrons (Γ and Γ_r, respectively) is illustrated in Fig. 11. The comblike structure in the electron energy-loss spectrum results from the spectral property of the resonator that is nonlocal with respect to the interaction region, and is only accessible since the interaction

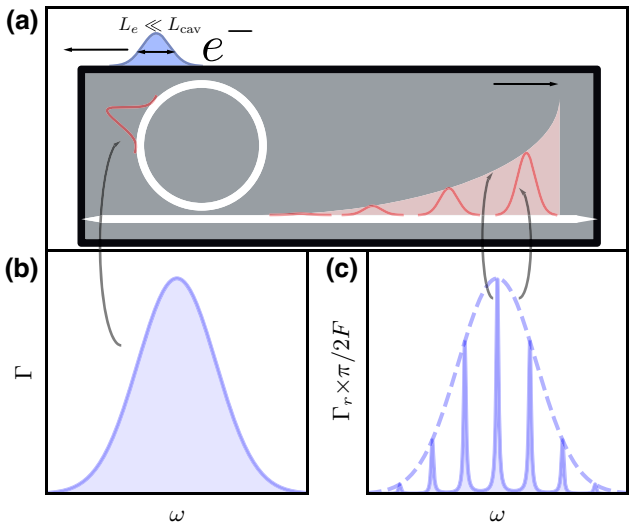

FIG. 11. Comparison between free electron coupling to waveguides versus resonators. (a) Illustration of electron-photon interaction mediated by an optical cavity. An optical pulse is first generated inside the cavity. Then the pulse circulates inside the cavity and couples out as a pulse train with repetition rate of FSR and an exponential decaying envelope. (b) Coupling spectrum for the pulse inside the resonator, indistinguishable to the one generated inside a waveguide with the same geometry. (c) Coupling spectrum for the out-coupled pulse trains, now exhibits a comblike feature with frequency spacing matching the resonator FSR, peak width matching the pulse-train envelope, and comb envelope matching the spectral components of each individual pulse.

is analyzed in the electron energy basis, whose state is also nonlocal in nature. However, in order to access these comblike features in an EELS experiment, the electron-cavity characteristic interaction time (determined by the measured electron ZLP) has to be longer than the round-trip time of the resonator, thus satisfying the energy-time uncertainty principle. Nonetheless, the comblike structure can always be accessed from the optical side with a measurement time longer than the round-trip time, as was shown in Ref. [46].

There is also no difference in the total coupling strength in a given mode family for the open waveguide case and the resonator case, as long as the the phase-matching bandwidth $\Delta\nu$ is much larger than $\Delta\nu_{\mathrm{FSR}}$. The total interaction strength $|g_m|^2$ of a mode family will be considerably altered by the resonator structure when the phase-matching bandwidth $\Delta\nu$ is on the frequency scale of one FSR. The minimum number of modes inside the phase-matching bandwidth can be estimated with $N \sim \frac{1}{|n_g - n_{\mathrm{eff}}|}$ (for common dielectric materials approximately 5–20), so in order to access the regime where the phase-matching bandwidth is smaller than the FSR, one requires $|n_g - n_{\mathrm{eff}}| > 1$, which is generally very difficult to achieve with structures using only dielectric materials. However, with common dielectric structures and careful mode dispersion engineering, the regime $N = \mathcal{O}(1)$ where the resonance structure has a small impact is accessible.

The motivation of using a resonator instead of an open waveguide is that the optical resonance frequencies are more passively stable, and the wavepackets generated from each resonator mode are generally much longer than the optical pulse length enforced by the phase-matching bandwidth from an open waveguide, and have energy density enhanced by the cavity finesse at resonant frequencies. Therefore, resonators have advantages in experiments where optical excitation needs to interfere with a reference local oscillator, and good mode matching is required. Resonators also provide advantages in experiments where optical frequency filtering is required, since the optical density of the excitation is concentrated in frequency. We show a frequency conversion example in Appendix L to exploit this advantage of optical resonators to convert THz broad optical excitation to MHz broad optical or microwave excitation, useful to bridge interactions with superconducting qubits, mechanical oscillators and long-life-time optical qubits.

APPENDIX G: PURITY AND FIDELITY OF HERALDED OPTICAL QUANTUM STATES

In this section, we derive the heralded optical states by measuring electron energy, and calculate the state fidelity and purity. The optical state generated when there is no sideband overlap (not a fundamental limit), and when conditioning on a narrow bandwidth around an energy slice $E_c \sim N\hbar\omega$ is

$$|\psi_{\mathrm{ph}}\rangle = \frac{\int \prod_{k=1}^{N} d\omega_k g^*_{\omega_k} \psi\left(E + \hbar(\sum_k \omega_k)\right) \hat{a}^\dagger_{\omega_k}|0\rangle}{\sqrt{\int \prod_{k=1}^{N} d\omega_k |g_{\omega_k}|^2 |\psi\left(E + \hbar(\sum_k \omega_k)\right)|^2 (N!)^2}}.$$

As one can see, the coefficient is a product between the electron wave function and the coupling coefficient. This reflects on the fact that the electron energy distribution is correlated with the frequency at which the photon is created. One will see later that this is not the case for conditional electron states, since in the no-recoil limit the frequency of the photon does not depend on the energy of the electron.

In the first limit when electron ZLP is much narrower than phase-matching bandwidth, we can simplify the expression to

$$|\psi_{\mathrm{ph}}\rangle = \frac{\int \prod_{k=1}^{N} d\omega_k \psi\left(E + \hbar(\sum_k \omega_k)\right) \hat{a}^\dagger_{\omega_k}|0\rangle}{\sqrt{\int \prod_{k=1}^{N} d\omega_k |\psi\left(E + \hbar(\sum_k \omega_k)\right)|^2 (N!)^2}}.$$

for single-photon states. The frequency components of the generated state are directly linked to $\phi(\omega) \propto \psi(E_c + \hbar\omega)$. Ignoring the waveguide dispersion during propagation, we have the optical waveform

$$\phi(T = t - z_\parallel/v) = \widetilde{\psi}(T) e^{i\omega_c T},$$

where it has a center frequency determined by the conditional electron energy, and an envelope profile that is exactly the time-domain electron spatial profile $\widetilde{\psi}(T)$. Therefore, by shaping electron wave functions and conditioning on the selected sideband energy, one can transfer the electron spatial wave function to the optical waveform of the photonic state at a desired optical frequency. For readers familiar with optical spontaneous parametric down-conversion, a similar technique is also used in heralded single-photon sources [128] to imprint the waveform of the pump field onto the signal field.

For conditional multiphoton optical states, as one can immediately see from the expression, since the electron wave function generally cannot be factorized to N components $\psi(E + \hbar(\sum_k \omega_k) \neq \prod_k F(E, \omega_k)$, the conditional state can not be addressed into a Fock state of a well-defined spatial-temporal mode, but since high phase-matching bandwidth usually comes with low g, we restrict ourselves to single-photon states in this limit.

We define the fidelity of the heralded single-photon state as

$$\mathcal{F} = \left|\langle\psi'_{\mathrm{ph}}|\psi_{\mathrm{ph}}\rangle\right|^2 = \frac{\left|\int d\omega g_\omega |\psi(E + \hbar\omega)|^2\right|^2}{\left(\int d\omega |g_\omega|^2 |\psi(E + \hbar\omega)|^2\right)\left(\int d\omega |\psi(E + \hbar\omega)|^2\right)}.$$

For the case of long propagation, we usually end up with very narrow phase-matching bandwidth and high interaction g. In this case, when conditioning on the Nth energy sideband, we can simplify the expression to

$$|\psi_{\rm ph}\rangle = \frac{\int \prod_{k=1}^{N} d\omega_k g^*_{\omega_k} \hat{a}^\dagger_{\omega_k}|0\rangle}{\sqrt{\int \prod_{k=1}^{N} d\omega_k |g_{\omega_k}|^2 (N!)^2}},$$

where it is a well-defined N-photon Fock state with mode profile $\phi(t)$ (see Appendix I), which is determined by both the waveguide routing and the material dispersion. To this end, one can adapt the electron positioning and velocity to shape the optical waveform.

We define the fidelity to this state as

$$\mathcal{F} = \left|\langle\psi'_{\rm ph}|\psi_{\rm ph}\rangle\right|^2 = \frac{\left|\int \prod_{k=1}^{N} d\omega_k |g_{\omega_k}|^2 \psi\left(E + \hbar(\sum_k \omega_k)\right)\right|^2}{\left(\int \prod_{k=1}^{N} d\omega_k |g_{\omega_k}|^2\right)\left(\int \prod_{k=1}^{N} d\omega_k |g_{\omega_k}|^2 |\psi\left(E + \hbar(\sum_k \omega_k)\right)|^2\right)}.$$

With more electron operation stages, we can select the electron measurement basis. After the pair-state generation, if we pass the electron through, e.g., a PINEM interaction stage characterized by the scattering matrix $\mathcal{S}(\alpha)$, by conditioning on the energy sideband $|E\rangle$, we are effectively measuring under the basis $\mathcal{S}^\dagger(\alpha)|E\rangle = \sum_i c_i^*|E_i\rangle$. Formally, we write down the conditional optical state as

$$|\psi_{\rm ph}\rangle \propto \sum_N \frac{c_N g^N}{\sqrt{N!}}|N\rangle,$$
$$\hat{\rho}_{\rm ph} = \langle E|\mathcal{S}(\alpha)\hat{\rho}\mathcal{S}^\dagger(\alpha)|E\rangle,$$

where $|g|^2 = \int d\omega |g_\omega|^2$. This effectively projects the optical state into a more general state other than Fock states if one directly measures the electron energy after the pair-state preparation. For these general states, the corresponding heralded state fidelity is an average of all the involved Fock states with a correct weight

$$\mathcal{F} = \left|\langle\psi'_{\rm ph}|\psi_{\rm ph}\rangle\right|^2 = \left|e^{-|g|^2}\sum_N \frac{|c_N|^2|g|^{2N}}{N!}\frac{\int \prod_{k=1}^{N} d\omega_k |g_{\omega_k}|^2 \psi\left(E_N + \hbar(\sum_k \omega_k)\right)}{\sqrt{\left(\int \prod_{k=1}^{N} d\omega_k |g_{\omega_k}|^2\right)\left(\int \prod_{k=1}^{N} d\omega_k |g_{\omega_k}|^2 |\psi\left(E_N + \hbar(\sum_k \omega_k)\right)|^2\right)}}\right|^2$$

and the same kind of weighted averaging needs to be applied to the heralded state purity as well.

The single-photon state purity can be degraded by two main effects. First, spectral overlap between different sideband orders. Second, relative bandwidth ratio between ZLP and phase-matching bandwidth. For higher-order Fock states, it is further affected by the spectral distribution of the other optical mode families as well, e.g., the electron might not be able to distinguish between a two-photon transition of the fundamental optical mode, and a single-photon transition of a higher-order mode. Here, we categorize this case into the spectral overlap between electron sidebands.

First, let us investigate the purity degradation of the conditional photonic Fock state due to the sideband spectral overlap. In the limit of narrow phase-matching bandwidth, the optical density matrix after detection at electron energy band ΔE electron energy event, is

$$\hat{\rho}_{\rm ph} = \frac{1}{\sum_N \frac{(\int d\omega |g_\omega|^2)^N}{N!}\int_{\Delta E} dE|\psi(E + N\hbar\omega)|^2}\int_{\Delta E} dE\left(\sum_N \frac{(-\int d\omega g^*_\omega \hat{a}^\dagger_\omega)^N}{N!}\prod_\omega |0_\omega\rangle\psi(E + N\hbar\omega)\right)$$
$$\times\left(\sum_N \psi^*(E + N\hbar\omega)\prod_\omega \langle 0_\omega|\frac{(-\int d\omega g_\omega \hat{a}_\omega)^N}{N!}\right).$$

The purity of this state is

$$\mathrm{Tr}\left[\hat{\rho}^2_{\rm ph}\right] = \frac{\sum_{N,N'}\frac{(\int d\omega |g_\omega|^2)^{N+N'}}{N!N'!}\iint_{\Delta E} dEdE'\psi(E + N\hbar\omega)\psi^*(E + N'\hbar\omega)\psi^*(E' + N\hbar\omega)\psi(E' + N'\hbar\omega)}{\left(\sum_N \frac{(\int d\omega |g_\omega|^2)^N}{N!}\int_{\Delta E} dE|\psi(E + N\hbar\omega)|^2\right)^2}.$$

Then we investigate the effect of finite phase-matching bandwidth, and in the limit where there is no photon sideband overlaps, the conditional single-photon Fock state is

$$\hat{\rho}_{\mathrm{ph}} = \frac{1}{\iint_{\Delta E} dE d\omega |g_\omega|^2 |\psi(E+\hbar\omega)|^2} \int_{\Delta E} dE \left(\int d\omega g_\omega^* \psi(E+\hbar\omega) \hat{a}_\omega^\dagger |0\rangle \right) \left(\int d\omega g_\omega \psi^*(E+\hbar\omega) \langle 0|\hat{a}_\omega \right),$$

with corresponding state purity

$$\mathrm{Tr}\left[\hat{\rho}_{\mathrm{ph}}^2\right] = \frac{\iint_{\Delta E} dE dE' d\omega d\omega' |g_\omega|^2 |g_{\omega'}|^2 \psi(E+\hbar\omega)\psi^*(E+\hbar\omega')\psi^*(E'+\hbar\omega)\psi(E'+\hbar\omega')}{\left(\iint_{\Delta E} dE d\omega |g_\omega|^2 |\psi(E+\hbar\omega)|^2\right)^2}.$$

In the limit of perfect electron energy resolution $\Delta E \to 0$, $\mathrm{Tr}\left[\hat{\rho}_{\mathrm{ph}}^2\right] \to 1$. However, experimentally, either the ZLP consists of a statistical uncertainty, or the conditioning window cannot be set arbitrarily small, due to its effect on the heralding rate. As a result, the purity is limited by both the phase-matching bandwidth, and the relative heralding bandwidth.

For a general N-photon Fock state, the density matrix of the heralded state is

$$\hat{\rho}_{\mathrm{ph}} = \frac{1}{\iint_{\Delta E} dE \prod_{k=1}^N d\omega_k |g_{\omega_k}|^2 |\psi\left(E+\hbar(\sum_k \omega_k)\right)|^2 (N!)^2} \int_{\Delta E} dE \left(\int \prod_{k=1}^N d\omega_k g_{\omega_k}^* \psi\left(E+\hbar(\sum_k \omega_k)\right) \hat{a}_{\omega_k}^\dagger |0\rangle \right)$$
$$\times \left(\int \prod_{k=1}^N d\omega_k g_{\omega_k} \psi^*\left(E+\hbar(\sum_k \omega_k)\right) \langle 0|\hat{a}_{\omega_k} \right)$$

with the corresponding state purity

$$\mathrm{Tr}\left[\hat{\rho}_{\mathrm{ph}}^2\right]$$
$$= \frac{\iint_{\Delta E} dE dE' \prod_{i,j=1}^N d\omega_i d\omega_j' |g_{\omega_i}|^2 |g_{\omega_j'}|^2 \psi\left(E+\hbar(\sum_i \omega_i)\right) \psi^*\left(E+\hbar(\sum_j \omega_j')\right) \psi^*\left(E'+\hbar(\sum_i \omega_i)\right) \psi\left(E'+\hbar(\sum_j \omega_j')\right)}{\left(\iint_{\Delta E} dE \prod_{i=1}^N d\omega_i |g_{\omega_i}|^2 |\psi\left(E+\hbar(\sum_i \omega_i)\right)|^2\right)^2}$$

To illustrate the impact of relative heralding bandwidth on state purity, we show the overall scaling of $1-\mathcal{P} \propto \gamma^2$ in the limit of small heralding bandwidth in Fig. 12. For a general state $|\psi_{\mathrm{ph}}\rangle = \sum c_N |N\rangle$, which consists of a coherent superposition of different Fock states $|N\rangle$, as discussed before in the state fidelity calculation, the purity is a $|c_N|^2$ weighted average of each individual Fock state component, shown as

$$\mathrm{Tr}\left[\hat{\rho}_{\mathrm{ph}}^2\right] = \sum_N |c_N|^4 \mathcal{P}_N + \sum_{N,N'} |c_N|^2 |c_{N'}|^2 \mathcal{P}_{N,N'}$$
$$\mathcal{P}_{N,N'} = \left(\iint_{\Delta E} dE dE' \prod_{i=1}^N \prod_{j=1}^{N'} d\omega_i d\omega_j' |g_{\omega_i}|^2 |g_{\omega_j'}|^2 \psi\left(E+\hbar(\sum_i \omega_i - N\overline{\omega})\right) \psi^*\left(E+\hbar(\sum_j \omega_j' - N'\overline{\omega})\right) \right.$$
$$\left. \times \psi^*\left(E'+\hbar(\sum_i \omega_i - N\overline{\omega})\right) \psi\left(E'+\hbar(\sum_j \omega_j' - N'\overline{\omega})\right) \right)$$
$$\times \left(\iint_{\Delta E} dE \prod_{i=1}^N d\omega_i |g_{\omega_i}|^2 |\psi\left(E+\hbar(\sum_i \omega_i - N\overline{\omega})\right)|^2 \right)^{-1}$$
$$\times \left(\iint_{\Delta E} dE \prod_{j=1}^{N'} d\omega_j' |g_{\omega_j'}|^2 |\psi\left(E+\hbar\left(\sum_j \omega_j' - N'\overline{\omega}\right)\right)|^2 \right)^{-1},$$

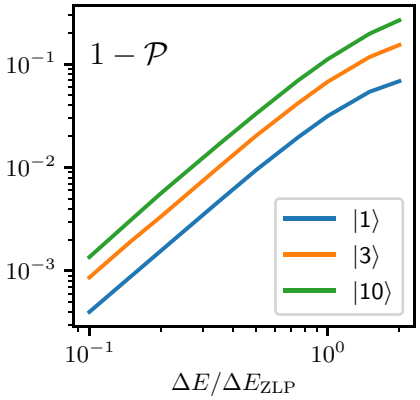

FIG. 12. Heralded optical state purity versus relative heralding bandwidth at different Fock-state basis. Here we assume 20-μm interaction length.

where $\mathcal{P}_N$ is the purity of the Nth Fock-state component, $\mathcal{P}_{N,N'}$ is the purity of the off-diagonal terms, and $\overline{\omega}$ is the center frequency of the optical state.

APPENDIX H: PURITY OF HERALDED ELECTRON STATE

In this section, we consider heralding schemes that generate complex electron states, and derive the expression of purity of the heralded electron state by the optical measurement. With multiple single-photon detectors, if one conditions on a N-photon counting event, one projects the electron into a corresponding energy state that loses an equal amount of energy. However, these types of photon-counting measurements cannot project the electron into a coherent superposition of multiple sideband states. This is the result of the chosen measurement operator $a^\dagger a$, whose eigenstates are Fock states. However, one can select a measurement basis to project the electron onto a more general state. These operations require high detection efficiencies (no information loss), which has to be considered carefully when applying optical elements, e.g., spectral filters. The first simple method to change the measurement basis would be to combine the signal with a strong local oscillator through a high-aspect-ratio beam splitter. This modifies the detection from photon-number detection to field detection in the basis of displaced Fock states. With the ability to mode match to an optical reference field, homodyne types of detection can also be realized. In the setting where the signal field is split and detected by two homodyne in orthogonal quadratures, the measurement is effectively under the coherent-state basis. More sophisticated operation can be done with an atomic system to provide arbitrary measurement basis.

In the special case of measuring in coherent-state basis $|\alpha\rangle = \sum_N c_N^* |N\rangle = e^{-|\alpha|^2/2} \sum_N \frac{\alpha^N}{\sqrt{N!}} |N\rangle$ (scheme see Appendix K), we can derive the effective modulation applied on the electron wave function as

$$A(z) = \sum_N \frac{c_N g^N}{\sqrt{N!}} e^{iN\frac{\omega}{v}z} \propto \sum_N \frac{(g\alpha^* e^{i\frac{\omega}{v}z})^N}{N!} = e^{g\alpha^* e^{i\frac{\omega}{v}z}},$$

which is effectively a direct density modulation of

$$|A(z)|^2 \propto e^{2|g\alpha^*|\cos(\frac{\omega}{v}z+\theta_{g\alpha})}.$$

Now, we consider a general heralded electron state, with the Nth sideband density-matrix component as

$$\hat{\rho}_e = \frac{1}{\iint_{\Delta\omega} dE \prod_{k=1}^N d\omega_k |g_{\omega_k}|^2 |\psi\left(E + \hbar(\sum_k \omega_k)\right)|^2} \times \int_{\Delta\omega} \prod_{k=1}^N d\omega_k |g_{\omega_k}|^2 \left(\int dE \psi(E) |E - \hbar(\sum_k \omega_k)\rangle\right) \times \left(\int dE \psi^*(E) \langle E - \hbar(\sum_k \omega_k)|\right).$$

Note that for each sideband component, the corresponding electron wave function is not shaped by the optical detection and maintains the original shape. This is in sharp contrast to heralding optical state by measuring electron energies. The difference is that the electron energy loss heavily depends on optical frequency, but the optical frequency does not depend on electron energy under the no-recoil approximation. Therefore, any measurement on the frequency of the created photons simply translates the original electron energy state down by a corresponding photon energy. Because of that, we do not define the fidelity of the electron wave function in the limit of perfect photon-frequency resolution.

We proceed to calculate the state purity of the Nth electron sideband component as

$$\mathrm{Tr}\left[\hat{\rho}_e^2\right] = \frac{\iint_{\Delta\omega} dE dE' \prod_{i,j=1}^N d\omega_i d\omega_j' |g_{\omega_i}|^2 |g_{\omega_j'}|^2 \psi\left(E + \hbar(\sum_i \omega_i)\right) \psi^*\left(E + \hbar(\sum_j \omega_j')\right) \psi^*\left(E' + \hbar(\sum_i \omega_i)\right) \psi\left(E' + \hbar(\sum_j \omega_j')\right)}{\left(\iint_{\Delta\omega} dE \prod_{i=1}^N d\omega_i |g_{\omega_i}|^2 |\psi\left(E + \hbar(\sum_i \omega_i)\right)|^2\right)^2},$$

where the same weighted average needs to be applied for a general state with weights $|c_N|^2$, similar to the case of heralded optical states.

APPENDIX I: OPTICAL WAVEFORM GENERATED FROM THE ELECTRON-PHOTON INTERACTION

In this section, we derive the waveform of the conditional optical state when considering the waveguide dispersion.

The composite quantum state after the electron-photon interaction is

$$\begin{aligned}|\psi\rangle &= \exp\left(\int d\omega g_\omega \hat{b}_\omega^\dagger \hat{a}_\omega - \text{h.c.}\right)|\psi_e\rangle|0\rangle \\ &= e^{-\frac{\int d\omega |g_\omega|^2}{2}} e^{-\int d\omega g_\omega^* \hat{b}_\omega \hat{a}_\omega^\dagger} e^{\int d\omega g_\omega \hat{b}_\omega^\dagger \hat{a}_\omega}|\psi_e\rangle|0\rangle \\ &= e^{-\frac{\int d\omega |g_\omega|^2}{2}} e^{-\int d\omega g_\omega^* \hat{b}_\omega \hat{a}_\omega^\dagger}|\psi_e\rangle|0\rangle \\ &= e^{-\frac{\int d\omega |g_\omega|^2}{2}} \sum_N \frac{\left(-\int d\omega g_\omega^* \hat{b}_\omega \hat{a}_\omega^\dagger\right)^N}{N!}|\psi_e\rangle|0\rangle\end{aligned}$$

when conditioned on the nth energy sideband of the electron state (with electron ZLP much wider than the coupling bandwidth to the optical modes), the heralded optical state is

$$|\psi_{\text{ph}}\rangle \sim \left(-\int d\omega g_\omega^* \hat{a}_\omega^\dagger\right)^N |0\rangle.$$

When the interaction is dominated by the coupling to a single optical mode family, one can generate the Fock state of a well-defined spatial-temporal mode as

$$\begin{aligned}|\psi_{\text{ph}}\rangle &\sim \left(\hat{a}_m^\dagger\right)^N |0\rangle, \\ \hat{a}_m &= \int_{\Delta\omega_m} d\omega \phi_m(\omega)\hat{a}_\omega, \\ \phi_m(\omega) &= \frac{g_{\omega,m}^*}{g_m^*}.\end{aligned}$$

From these results, one can derive the temporal field profile function of this spatial-temporal mode, as it may concern experiments that require waveform shaping. Straight from the definition, one gets

$$\phi_m(\mathbf{r},t) \propto \iint dz d\omega e^{i\omega(z/v_e - t)} \tilde{U}_{m,z}^*(\mathbf{R}_0, z, \omega)\tilde{\mathbf{U}}_m(\mathbf{r},\omega).$$

When chromatic dispersion of the frequency modes is ignored, one retrieves the waveform shown in the main text. When dispersion is considered, one can further remove the frequency dependence of the mode profile functions by assuming an open waveguide (e.g., no sharp frequency response in the phase-matched region) and up to second-order dispersion β,

$$\tilde{\mathbf{U}}_m(\mathbf{r},\omega) \approx \tilde{\mathbf{U}}_m(\mathbf{r},\omega_m) e^{i(\omega-\omega_m)r_\parallel/v_g} e^{i\beta(\omega-\omega_m)^2 r_\parallel/v_g},$$

where ω_m is the center frequency of the pulse, selected so that the phase velocity at ω_m matches the electron velocity v, $v_g \lesssim v$ is the corresponding group velocity, and $r_\parallel$ is the longitudinal coordinate along the waveguide trajectory. One can then rewrite the expression as

$$\begin{aligned}\phi_m(\mathbf{r},t) &\propto \iint dz d\omega e^{i\frac{(\omega-\omega_m)}{v}\left(z-\frac{v}{v_g}(R_\parallel(z)-r_\parallel)-vt\right)} e^{i\beta\frac{(\omega-\omega_m)^2}{v_g}\left(r_\parallel - R_\parallel(z)\right)} e^{i\omega_m(z/v_e-t)} \tilde{U}_{m,z}^*(\mathbf{R}_0,z,\omega_m)\tilde{\mathbf{U}}_m(\mathbf{r},\omega_m) \\ &\propto \int dz e^{i\frac{\left(z-\frac{v}{v_g}\left(R_\parallel(z)-\tilde{r}_\parallel\right)\right)^2}{4\beta\left(r_\parallel - R_\parallel(z)\right)v^2/v_g}} \frac{e^{i\frac{\pi}{4}\text{sgn}\left(\beta\left(r_\parallel - R_\parallel(z)\right)\right)}}{\sqrt{|\beta\left(r_\parallel - R_\parallel(z)\right)|}} e^{i\omega_m(z/v_e-t)} \tilde{U}_{m,z}^*(\mathbf{R}_0,z,\omega_m)\tilde{\mathbf{U}}_m(\mathbf{r},\omega_m) \\ &\propto \int dz K(z,\mathbf{r},t)\overline{\tilde{U}}_{m,z}^*(\mathbf{R}_0,z,\omega_m)\tilde{\mathbf{U}}_m(\mathbf{r},\omega_m)e^{-i\omega_m t}\end{aligned}$$

where $\tilde{r}_\parallel \equiv r_\parallel - v_g t$ is the waveform coordinate in the optical pulse frame with group velocity v_g. $\overline{\tilde{U}}_{m,z}^*(\mathbf{R}_0,z,\omega_m)$ is the mode envelope profile at wave vector ω_m/v. The integral kernel

$$K(z,\mathbf{r},t) \equiv e^{i\frac{\left(z-\frac{v}{v_g}\left(R_\parallel(z)-\tilde{r}_\parallel\right)\right)^2}{4\beta\left(r_\parallel - R_\parallel(z)\right)v^2/v_g}} \frac{e^{i\frac{\pi}{4}\text{sgn}\left(\beta\left(r_\parallel - R_\parallel(z)\right)\right)}}{\sqrt{|\beta\left(r_\parallel - R_\parallel(z)\right)|}}$$

represents a phase scrambling around the waveform coordinate $\tilde{r}_\parallel$ with a bandwidth of approximately $|\beta(r_\parallel)v^2/v_g|$, due to the presence of second-order dispersion. One can get physical intuition of the waveform in the limit of weak dispersion ($\beta \to 0$), where one can approximate the integral kernel with a Dirac delta function,

$$\phi_m(\mathbf{r},t) \propto \int dz\delta\left(z - \frac{v}{v_g}\left(R_\parallel(z) - \tilde{r}_\parallel\right)\right)\overline{\tilde{U}}^*_{m,z}(\mathbf{R}_0,z,\omega_m)\tilde{\mathbf{U}}_m(\mathbf{r},\omega_m)e^{-i\omega_m t} \propto \sum_i \frac{\overline{\tilde{U}}^*_{m,z}(\mathbf{R}_0,z_i,\omega_m)}{\left|R_{\parallel\partial z}(z_i) - \frac{v_g}{v}\right|}\tilde{\mathbf{U}}_m(\mathbf{r},\omega_m)e^{-i\omega_m t}$$

where $z_i(\mathbf{r},t): \ \frac{z_i}{v} - \frac{1}{v_g}\left(R_\parallel(z_i) - \tilde{r}_\parallel\right) = 0$ are the spatial z coordinates where the vacuum field contributes the most through the phase-matching condition to the generated field at $\mathbf{r}$ coordinate at time t. Therefore, the excited optical profile in the time domain is easily connected to the envelope of the optical mode field profile $\tilde{U}_{m,z}(\mathbf{R}_0,z,\omega_m)$ along the electron propagation direction, when the mode dispersion is sufficiently weak. In the exact limit $\beta = 0$, there can be unphysical scenarios when $|R_{\parallel\partial z}(z_i) - \frac{v_g}{v}| = 0$, which corresponds to the infinite phase-matching bandwidth. However, in physical materials, the phase-matching bandwidth is always finite.

The mode dispersion during pulse propagation will cause pulse shortening or broadening by shifting the phase of different frequency components and leaving the amplitude unchanged. This can be easily corrected and is not a fundamental limit to construct an arbitrary waveform. Therefore, one can structure any desired optical waveform $\phi(\mathbf{r},t)$ by positioning the electron-beam trajectory on an optical waveguide with a tailormade waveguide structure.

APPENDIX J: IMPRINTING ELECTRON WAVE FUNCTION ONTO THE OPTICAL WAVEFORM IN AN INTERFEROMETRIC FASHION

In the regime where the electron energy spread is much narrower than the phase-matching bandwidth, the spatial-temporal mode is defined completely by the electron wave function, see Appendix G, with a phase contribution from the coupling coefficient $g_{\omega_c=-E_c/(N\hbar)}$, where N is the sideband order. Whenever an electron interacts with an optical mode, and measured on the Nth electron energy sideband at the energy E_c, it is equivalent to apply an operator $\hat{S} \propto \psi(E_c + \hbar\omega)\left(e^{i\theta_g}\hat{a}^\dagger_\omega\right)^N$ onto the optical state. When the electron interacts with two waveguides in sequential manner (identical geometry), the operator is

$$\hat{S} \propto \int d\omega\psi(E + \hbar\omega)\left(e^{i\theta_{g_1}}\hat{a}^\dagger_{1,\omega} + e^{i\theta_{g_2}}\hat{a}^\dagger_{2,\omega}\right)^N,$$

where a_i is the spatial-temporal mode on waveguide $i = 1,2$, and the phase is determined by the the reference point from both the optical side and the electron side. When the two interaction regimes (positions of waveguides) are separated by a spatial distance that correspond to an electron propagation time Δt, we have the following phase relation of the coupling coefficients

$$e^{-i\hat{H}_0\Delta t}\hat{S}_{e\text{-ph}}(g_\omega)e^{-i\hat{H}_0\Delta t} = \hat{S}_{e\text{-ph}}(g_\omega e^{i\omega\Delta t}),$$

where $\hat{H}_0$ is the electron free-evolution Hamiltonian. If we assume the optical phase references are set to 0, we can rewrite the scattering as

$$\hat{S} \propto \int d\omega\psi(E + \hbar\omega)\left(\hat{a}^\dagger_{1,\omega} + e^{i\omega\Delta t}\hat{a}^\dagger_{2,\omega}\right)^N.$$

As one can see, this interaction projects the optical state into a quantum coherent spatial superposition state of two spatially separated waveguides. In the case that the two waveguides are connected to a 50:50 beam splitter to form an interferometer, the photon flux difference $f(t)$ can be expressed as

$$f(t) \propto \mathrm{Re}\left[\widetilde{\psi}(t)\widetilde{\psi}^*(t + \Delta t)e^{i\omega_c\Delta t}\right],$$

which forms an effective optical interferometer of the time delay the electron experiences between two interaction stages, but can also be induced by an external potential. Here, to extract the delay time, one can simply look at the photon-counting record at different electron energy records E_c, which determines ω_c. Therefore, compared to conventional optical interferometry where one has to scan the laser frequency over a very broad range to resolve length difference to the order of a few wavelengths, here, we exploit the very wide electron emission bandwidth to get an accurate length difference, just by looking at different electron energy records. Note that here the imprinted electron wave function provides only a profile function with an effective optical delay (convenient for automatic mode matching between the two arms), with its original fast-evolving phase unobservable. Therefore, for a phase object positioned between the two waveguides, the interferometer sensitivity is on the optical wavelength scale, not on the scale of the de Broglie wavelength of the electrons.

APPENDIX K: OPTICAL DETECTION IN COHERENT-STATE BASIS

The scheme to conduct optical detection in the coherent-state basis is as follows: an arbitrary optical state $|\psi\rangle$ is passed to the input port 1 of a 50:50 beam splitter $\hat{U}_{\rm BS}$, with two output ports 1 and 2. Each output port is passed to a homodyne detection stage where orthogonal quadratures are measured. This two-quadrature measurement is then equivalent to projecting the input state into a coherent state. In the following, we first briefly review the quadrature projection in homodyne measurements, and then prove this claim.

Homodyne detection is conducted by interfering the signal field with a strong local oscillator field $|A\rangle$ at a balanced beam splitter, and the differential photon number at the two output ports is measured. It has been shown in Ref. [129] that this type of detection can be simplified as a quadrature-state projection, where there is a unique mapping $x = m/\sqrt{2}|A|$ between the differential photon number m and the measured quadrature state $|x\rangle_p$. The mapping requires the photon-number variance of the local oscillator field $|A\rangle$ to be much bigger than that of the optical state $|\psi\rangle$.

Therefore, the scheme effectively states that two orthogonal quadrature projections $|x_1\rangle_p \otimes |x_2\rangle_p$ at the two output ports of a beam splitter projects the input state into a coherent state $|\alpha\rangle$. We prove it by expressing a quadrature state as a function of creation operators acting on the vacuum state [130], as in

$$|x\rangle_p = \frac{e^{-x^2/2}}{\pi^{1/4}} e^{-\frac{\hat{a}^{\dagger 2}}{2} + \sqrt{2}x\hat{a}^\dagger}|0\rangle.$$

We also use the following relations:

$$\hat{U}^\dagger_{\rm BS}\hat{a}^\dagger_1\hat{U}_{\rm BS} = \frac{\hat{a}^\dagger_1 + i\hat{a}^\dagger_2}{\sqrt{2}}, \quad \hat{U}^\dagger_{\rm BS}\hat{a}^\dagger_2\hat{U}_{\rm BS} = \frac{i\hat{a}^\dagger_1 + \hat{a}^\dagger_2}{\sqrt{2}}.$$

Given the measurement results that the output ports are states $|x_1\rangle_p$ and $|x_2\rangle_p$, and a vacuum state $|0_2\rangle$ at the second input port, the conditional state at the first input port will be

$$\begin{aligned}
|\psi_c\rangle &= \langle 0_2|\hat{U}^\dagger_{\rm BS}|x_1\rangle_p|x_2\rangle_p = \langle 0_2|\hat{U}^\dagger_{\rm BS}\frac{e^{-(x_1+x_2)^2/2}}{\pi^{1/2}} \\
&\quad \times e^{-\frac{\hat{a}^{\dagger 2}_1 + \hat{a}^{\dagger 2}_2}{2} + \sqrt{2}(x_1\hat{a}^\dagger_1 + x_2\hat{a}^\dagger_2)}\hat{U}_{\rm BS}\hat{U}^\dagger_{\rm BS}|0_1\rangle|0_2\rangle \\
&= \frac{e^{-(x_1+x_2)^2/2}}{\pi^{1/2}}\langle 0_2|e^{-i\hat{a}^\dagger_1\hat{a}^\dagger_2 + (x_1+ix_2)\hat{a}^\dagger_1 + (ix_1+x_2)\hat{a}^\dagger_2}|0_1\rangle|0_2\rangle \\
&= \frac{e^{-(x_1+x_2)^2/2}}{\pi^{1/2}} e^{(x_1+ix_2)\hat{a}^\dagger_1}|0_1\rangle = \pi^{-1/2}\hat{D}(x_1+ix_2)|0_1\rangle \\
&= \pi^{-1/2}|\alpha_1 = x_1 + ix_2\rangle.
\end{aligned}$$

The factor of $\pi^{-1/2}$ comes from the overcompleteness of the coherent-state basis, as in

$$\begin{aligned}
1 &= \langle 0_2|\hat{U}^\dagger_{\rm BS}\left(\int dx_1dx_2|x_1\rangle_p\langle x_1|_p|x_2\rangle_p\langle x_2|_p\right)\hat{U}_{\rm BS}|0_2\rangle \\
&= \int dx_1dx_2\pi^{-1}|\alpha_1 = x_1 + ix_2\rangle\langle\alpha_1 = x_1 + ix_2| = 1.
\end{aligned}$$

As one can see, the conditioning of a coherent state comes from the cancelation of second-order term $\hat{a}^{\dagger 2}$ due to the even splitting ratio of the beam splitter and a correct phase relation. If this requirement is not met, it will result in a squeezed coherent state as the conditional state, e.g., for a beam splitter with a transmission of η,

$$|\psi_c\rangle = \frac{e^{-(x_1+x_2)^2/2}}{\pi^{1/2}} e^{\frac{(2\eta-1)\hat{a}^{\dagger 2}_1}{2} + \sqrt{2}(\sqrt{\eta}x_1 + i\sqrt{1-\eta}x_2)\hat{a}^\dagger_1}|0_1\rangle.$$

APPENDIX L: FREQUENCY CONVERSION USING RESONATOR STRUCTURES

As discussed in the previous section, optical resonators provide unique advantages over straight waveguides in terms of the concentrated optical density. Here we show an example scheme to use on-chip ring-resonator structures to convert the THz-broad optical excitation from the electron-photon interaction to a MHz-broad optical and electrical excitation, limited by the optical resonator linewidth. Here we define the spatial-temporal mode for the optical excitation of a resonator as $\hat{a}^\dagger = \int d\omega \sum_i \phi_i(\omega)\hat{a}^\dagger_\omega$, where each $\phi_i(\omega)$ is a Lorentzian centered around $\omega_i + \omega_m$ with ω_i the pump center frequency. We also define the microwave excitation as $\hat{c}^\dagger \propto \int d\omega\phi(\omega)\hat{c}^\dagger_\omega$, centered around ω_m. In the ideal case that all the optical azimuthal modes are identical in their frequency components, we have $\phi_i(\omega + \omega_i) = \phi(\omega)$.

Near-unity efficiency optical to microwave conversion is demonstrated in χ_2-type materials [98,99]. We assume a ring-structure optical resonator (conversion ring) with a strong χ_2 nonlinearity and a relatively high optical quality factor, with identical cavity azimuthal modes of two orthogonal polarizations (e.g., TE and TM fundamental modes) with approximately the same FSR, and a frequency spacing approximately ω_m between these two mode families that matches the microwave mode frequency ω_m. Practically, the frequency matching is only required between a few optical resonances, since the electron-photon optical excitation from a ring resonator can occupy only 5–20 azimuthal modes. We use this resonator for frequency down-conversion of the broadband photon excitation $\hat{a}^\dagger$ at frequencies $\omega_i + \omega_m$ from the electron-photon interaction, with a specially structured local-oscillator pump at frequencies ω_i. We further assume that there are two more rings on the chip, with matched optical frequencies of the modes of interest. We use one of the rings for

electron-photon interaction, where the photon excitation is generated on the TM polarization at frequencies $\omega_i + \omega_m$ (signal field). This ring should be designed with the highest quality factor possible, since its linewidth determines the microwave linewidth $\phi(\omega)$, and should be narrower than the linewidth of the conversion ring. We use the other ring for generating or filtering a structured cw optical pump on the TE polarization with frequencies ω_i (LO field). We combine LO and signal field through a polarization beam splitter, and send them into the conversion ring for frequency down-conversion.

In principle, the signal field and LO field does not have to be orthogonal in polarization to enable efficient and low-noise frequency conversion. The orthogonal polarizations considered here are intended to prevent spectral leakage of the LO field to the signal mode, even though they can be sufficiently separated in frequency.

When the conversion ring is pumped by the LO field with cooperativity $C = 1$ in each pump-field mode pairs, the signal frequency component $\phi_i(\omega)$ at the azimuthal mode at frequency $\omega_i + \omega_m$ is converted to a microwave photon at frequency ω_m with frequency component $\phi(\omega)$ and conversion efficiency $\eta = 100\%$. When all the azimuthal modes of the conversion ring convert their signal field components down to the same microwave frequency ω_m with unity efficiencies, the original signal pulse with THz-broad frequency components from the electron-photon interaction will be converted to a single microwave mode excitation at frequency ω_m with frequency width down to MHz with a unity efficiency, and at the same time generate a pump field photon with THz-broad frequency component due to the energy conservation.

Here, we formally analyze this conversion process. We define the scattering matrix of the conversion process with a multimode three-wave mixing operator

$$\hat{S}_{\mathrm{TWM}} = e^{\sum_i \int \beta_i(\omega,\omega_i)\hat{a}_{\omega+\omega_i}\hat{c}^\dagger_\omega \hat{d}^\dagger_{\omega_i} - \mathrm{h.c.}},$$

where ω_i is the frequency of each cw pump comb tooth, and β_i the coupling constant amplified by the pump field. The coupling constant $\beta_i(\omega, \omega_i)$ contains the conversion frequency response of each pump-signal mode pair, including effects, e.g., phase-matching, cavity responses of the signal and pump field, and microwave cavity response. The operators are the signal field annihilation $\hat{a}_\omega$, the microwave field creation operator $\hat{c}^\dagger_\omega$, and the pump field operator $\hat{d}^\dagger_{\omega_i} = \sum_{N_{\omega_i}} |N_{\omega_i}+1\rangle\langle N_{\omega_i}|$, which is specially defined high up in the photon ladder, similar to the electron ladder operator in the no-recoil limit, that represents the addition of a photon to the classical coherent pump field $|\alpha_i\rangle$ with frequency ω_i. In the single-mode conversion case, $\hat{d}^\dagger$ can be ignored. However, in the multimode conversion considered here, neglecting $\hat{d}^\dagger$ leads to nonunitary operations. Under such an operation, the state of the system changes to

$$\hat{S}_{\mathrm{TWM}}|\psi_{\mathrm{ph}}, \psi_m, \psi_{\mathrm{pump}}\rangle = \hat{S}_{\mathrm{TWM}} F(\hat{a}^\dagger)|0_a, 0_c, \alpha_i\rangle = F(\hat{S}_{\mathrm{TWM}}\hat{a}^\dagger\hat{S}^\dagger_{\mathrm{TWM}})\hat{S}_{\mathrm{TWM}}|0_a, 0_c, \alpha_i\rangle = F(\hat{S}_{\mathrm{TWM}}\hat{a}^\dagger\hat{S}^\dagger_{\mathrm{TWM}})|0_a, 0_c, \alpha_i\rangle$$

$$\hat{S}_{\mathrm{TWM}}\hat{a}^\dagger\hat{S}^\dagger_{\mathrm{TWM}} = \sum_i \phi_i(\omega+\omega_i)\sin(|\beta_i(\omega,\omega_i)|)e^{i\theta_i}\hat{d}^\dagger_{\omega_i}\hat{c}^\dagger_\omega + \sum_i \phi_i(\omega)\cos(|\beta_i(\omega-\omega_i,\omega_i)|)\hat{a}^\dagger_\omega,$$

where $\hat{a}^\dagger = \int d\omega \sum_i \phi_i(\omega)\hat{a}^\dagger_\omega$ is used, $\theta_i = \arg[\beta_i(\omega,\omega_i)]$, and also $|\psi_{\mathrm{ph}}\rangle = F(\hat{a}^\dagger)|0_a\rangle$. In the ideal case where $\phi_i(\omega + \omega_i) = \phi(\omega)G_i$ is separated to the cavity density of states $\phi(\omega)$ and the electron-photon phase-matching coefficient G_i at signal mode i, with unity cooperativity $\beta_i(\omega,\omega_i) = \pi/2$ at every pump-signal mode pair over the frequency components of interest, the state is simplified to

$$|\psi_m, \psi_{\mathrm{pump}}\rangle = F(\hat{c}^\dagger\hat{d}^\dagger)|0_c, \alpha_i\rangle,$$

where

$$\hat{c}^\dagger = \int d\omega \sqrt{\sum_i |G_i|^2}\phi(\omega)\hat{c}^\dagger_\omega,$$

$$\hat{d}^\dagger = \sum_i \frac{G_i}{\sqrt{\sum_i |G_i|^2}} e^{i\theta_i}\hat{b}^\dagger_{\omega_i}.$$

Since the pump field is a strong coherent field and maintains a unity overlap with a photon-added state, we can trace out the pump-field state space, and arrive at

$$|\psi_m\rangle = F(\hat{c}^\dagger)|0_c\rangle,$$

where the state of the signal field $|\psi_{\mathrm{ph}}\rangle = F(\hat{a}^\dagger)|0_a\rangle$ is transferred to the microwave field, with frequency components limited by the signal cavity density of states $\propto \phi(\omega)$.

Practically, the amplitude and frequency components of the LO field has to be specifically shaped, but since the optical excitation from the electron-photon interaction can occupy only 5–20 optical modes with the maximum interaction length achievable with a racetrack resonator geometry, it is possible to shape a reasonably accurate LO field with a soliton [92] or an electro-optic comb [93] source and a frequency shaper [94].

There are currently two types of main-stream optical-to-microwave converters [3]. One type uses χ_2 optical nonlinearity to directly convert signals from the optical domain to the microwave domain, as is considered here. The other type [131] uses a mechanical oscillator as an intermediate stage to first convert the optical signal to a mechanical signal using optomechanical couplings, and then from the mechanical signal to a microwave signal using electromechanical couplings. Both types of systems have shown near-unity conversion efficiency and low added noise, but the mechanical one suffers from the low-conversion bandwidth typically at kHz level [not possible to achieve $\beta_i(\omega,\omega_i)\sim\pi/2$ over the cavity bandwidth approximately MHz], limited by the electromechanical and optomechanical coupling rates. Therefore, we consider only χ_2-type optical-to-microwave converters for our scheme since they offer broadband transductions, essential to convert all the frequency components of the optical excitation to the microwave domain. For realistic lithium-niobate ring resonators with 50-μm radius, the microwave frequency at 4 GHz, with optical and microwave cavity linewidths at $\kappa_{\mathrm{ph}/m}/2\pi\sim 10$ MHz, the estimated required pump power to reach $C_i=1$ is reasonable at $P_i\sim 100\,\mu\mathrm{W}$ [132].

Similar types of schemes can also down-convert the signal to an optical excitation with MHz linewidth. But generally, a relatively uniform mode spacing over multiple azimuthal modes at optical frequency scale is harder to design for triply resonant schemes.

APPENDIX M: BEYOND NO-RECOIL APPROXIMATION

In the no-recoil limit, the coupling coefficient g_ω is not energy dependent, as is the case for the scenarios we discuss in the current study. However, the recoil effect will be significant with multistage operations with sufficient spatial separation, where the effect of electron energy-momentum dispersion kicks in.

Here, we consider two stages separated by distance ΔL, with near-point-like interaction regions. The coupling coefficient for the first stage is

$$g_{1,\omega}\propto\int dz e^{-i\frac{\omega}{v}z}U_{1,z}(z),$$

where $U_{1,z}(z)$ is the optical mode function along $\hat{z}$ direction. At the first stage the recoil effect does not play a significant role yet. However, at the second stage that is ΔL away, the electron energy dispersion $\hbar k=\sqrt{E^2/c^2-m^2c^2}$ changes the phase-matching integral of the off-diagonal element $|E+\hbar\omega\rangle\langle E|$ to

$$\begin{aligned}g_{2,\omega}(\Delta E=E-E_0)&\propto\int dz e^{-i\left(\frac{\omega}{v}-2\pi\left(\frac{2\Delta E}{\hbar\omega}+1\right)\frac{1}{z_T}\right)z}U_{2,z}(z)\\&\approx e^{i2\pi\left(\frac{2\Delta E}{\hbar\omega}+1\right)\frac{\Delta L}{z_T}}\int dz e^{-i\frac{\omega}{v}z}U_{2,z}(z),\end{aligned}$$

where now the coupling coefficient accumulates an energy-dependent phase $e^{i2\pi(\frac{2\Delta E}{\hbar\omega}+1)\frac{\Delta L}{z_T}}$. Here $z_T=4\pi mv^3\gamma^3/\hbar\omega^2$ is the Talbot distance [133] and γ is the Lorentz factor. ΔE is the distance to the original center electron energy E_0, which is the reference point of the dispersion quadratic expansion. In the case of $v/c\sim 0.65$ and $\omega\sim 2\pi\times 2\times 10^{14}$ Hz, $z_T\sim 1$ m. For the largest photon number $|N=10\rangle$ discussed in the current paper, and a typical photonic chip length $\Delta L\sim 5$ mm, the phase accumulation is $\theta=0.1\times 2\pi$, therefore negligible in our discussion. We anticipate the effect to dominate, e.g., when two photonic chips are involved and with sufficient separation $\Delta L\sim 1$ m. When that is indeed the case, we can still use the scattering matrix with the no-recoil approximation (used in the current paper) at the second stage, but add a propagation matrix

$$\hat{S}_{\mathrm{prop}}=\int dE\exp\left[\frac{-i\Delta L(E-E_0)^2}{2\hbar mv^3\gamma^3}\right]|E\rangle\langle E|,$$

to account for the recoil-induced phase accumulation of different energy components when arriving at the second stage. The phases accumulate differently between different energy components due to their different group velocities, and therefore there is an effective timing difference of their arrival at the second stage, which is treated as a point interaction with no-recoil approximation. This is consistent with the literature that uses Schrödinger equations to solve for the wave-function evolution between two interaction stages [40], and can also explain effects observed in double-PINEM-type experiment [23].

However, our assumption of pointlike interaction will break down when a single interaction is sufficiently long, e.g., $L>10$ cm, and with transitions involving Fock states $|N>10\rangle$. Then a single scattering matrix including the recoil effect has to be used to account for the dispersive phase accumulation during the interaction, as

$$\tilde{\hat{S}}_{e\text{-ph}}=\exp\left[\int d\omega g_\omega\tilde{\hat{b}}_\omega^\dagger\hat{a}_\omega-\mathrm{h.c.}\right],$$

where the modified electron energy lowering operator is

$$\tilde{\hat{b}}_\omega=\int dE|E\rangle\langle E+\hbar\omega|\frac{\int dz e^{i\left(\frac{\omega}{v}-2\pi\left(\frac{2(E-E_0)}{\hbar\omega}+1\right)\frac{1}{z_T}\right)z}U_z^*(z)}{\int dz e^{i\frac{\omega}{v}z}U_z^*(z)}$$

and the no-recoil coupling coefficient g_ω is used. For nonguided electron beam with divergence angle around

0.2 mrad, and an electron-surface gap 100 nm, the longest propagation on chip is restricted to about 1 mm. To achieve long enough distance such that recoil effect kicks in, an on-chip electron guiding structure [36,77] is required.

[1] H. J. Kimble, The quantum internet, Nature **453**, 1023 (2008).

[2] M. Wallquist, K. Hammerer, P. Rabl, M. Lukin, and P. Zoller, Hybrid quantum devices and quantum engineering, Phys. Scr. **2009**, 014001 (2009).

[3] D. Awschalom, *et al.*, Development of Quantum Interconnects (QuICs) for Next-Generation Information Technologies, PRX Quantum **2**, 017002 (2021).

[4] M. Mirhosseini, A. Sipahigil, M. Kalaee, and O. Painter, Superconducting qubit to optical photon transduction, Nature **588**, 599 (2020).

[5] R. W. Andrews, R. W. Peterson, T. P. Purdy, K. Cicak, R. W. Simmonds, C. A. Regal, and K. W. Lehnert, Bidirectional and efficient conversion between microwave and optical light, Nat. Phys. **10**, 321 (2014).

[6] A. Sipahigil, R. E. Evans, D. D. Sukachev, M. J. Burek, J. Borregaard, M. K. Bhaskar, C. T. Nguyen, J. L. Pacheco, H. A. Atikian, C. Meuwly, R. M. Camacho, F. Jelezko, E. Bielejec, H. Park, M. Lončar, and M. D. Lukin, An integrated diamond nanophotonics platform for quantum-optical networks, Science **354**, 847 (2016).

[7] N. H. Wan, T.-J. Lu, K. C. Chen, M. P. Walsh, M. E. Trusheim, L. De Santis, E. A. Bersin, I. B. Harris, S. L. Mouradian, I. R. Christen, E. S. Bielejec, and D. Englund, Large-scale integration of artificial atoms in hybrid photonic circuits, Nature **583**, 226 (2020).

[8] G. S. MacCabe, H. Ren, J. Luo, J. D. Cohen, H. Zhou, A. Sipahigil, M. Mirhosseini, and O. Painter, Nano-acoustic resonator with ultralong phonon lifetime, Science **370**, 840 (2020).

[9] R. Riedinger, A. Wallucks, I. Marinković, C. Löschnauer, M. Aspelmeyer, S. Hong, and S. Gröblacher, Remote quantum entanglement between two micromechanical oscillators, Nature **556**, 473 (2018).

[10] C. Monroe, R. Raussendorf, A. Ruthven, K. R. Brown, P. Maunz, L.-M. Duan, and J. Kim, Large-scale modular quantum-computer architecture with atomic memory and photonic interconnects, Phys. Rev. A **89**, 022317 (2014).

[11] B. Brandstätter, A. McClung, K. Schüppert, B. Casabone, K. Friebe, A. Stute, P. O. Schmidt, C. Deutsch, J. Reichel, R. Blatt, and T. E. Northup, Integrated fiber-mirror ion trap for strong ion-cavity coupling, Rev. Sci. Instrum. **84**, 123104 (2013).

[12] I. Shomroni, S. Rosenblum, Y. Lovsky, O. Bechler, G. Guendelman, and B. Dayan, All-optical routing of single photons by a one-atom switch controlled by a single photon, Science **345**, 903 (2014).

[13] T. G. Tiecke, J. D. Thompson, N. P. de Leon, L. R. Liu, V. Vuletić, and M. D. Lukin, Nanophotonic quantum phase switch with a single atom, Nature **508**, 241 (2014).

[14] M. Brekenfeld, D. Niemietz, J. D. Christesen, and G. Rempe, A quantum network node with crossed optical fibre cavities, Nat. Phys. **16**, 647 (2020).

[15] B. Barwick, D. J. Flannigan, and A. H. Zewail, Photon-induced near-field electron microscopy, Nature **462**, 902 (2009).

[16] S. T. Park, M. Lin, and A. H. Zewail, Photon-induced near-field electron microscopy (PINEM): Theoretical and experimental, New J. Phys. **12**, 123028 (2010).

[17] F. J. García de Abajo, Optical excitations in electron microscopy, Rev. Mod. Phys. **82**, 209 (2010).

[18] A. Yurtsever, R. M. van der Veen, and A. H. Zewail, Subparticle ultrafast spectrum imaging in 4D electron microscopy, Science **335**, 59 (2012).

[19] J. Breuer and P. Hommelhoff, Laser-Based Acceleration of Nonrelativistic Electrons at a Dielectric Structure, Phys. Rev. Lett. **111**, 134803 (2013).

[20] E. A. Peralta, K. Soong, R. J. England, E. R. Colby, Z. Wu, B. Montazeri, C. McGuinness, J. McNeur, K. J. Leedle, D. Walz, E. B. Sozer, B. Cowan, B. Schwartz, G. Travish, and R. L. Byer, Demonstration of electron acceleration in a laser-driven dielectric microstructure, Nature **503**, 91 (2013).

[21] A. Feist, K. E. Echternkamp, J. Schauss, S. V. Yalunin, S. Schäfer, and C. Ropers, Quantum coherent optical phase modulation in an ultrafast transmission electron microscope, Nature **521**, 200 (2015).

[22] L. Piazza, T. Lummen, E. Quiñonez, Y. Murooka, B. Reed, B. Barwick, and F. Carbone, Simultaneous observation of the quantization and the interference pattern of a plasmonic near-field, Nat. Commun. **6**, 6407 (2015).

[23] K. E. Priebe, C. Rathje, S. V. Yalunin, T. Hohage, A. Feist, S. Schäfer, and C. Ropers, Attosecond electron pulse trains and quantum state reconstruction in ultrafast transmission electron microscopy, Nat. Photon. **11**, 793 (2017).

[24] K. Wang, R. Dahan, M. Shentcis, Y. Kauffmann, A. Ben Hayun, O. Reinhardt, S. Tsesses, and I. Kaminer, Coherent interaction between free electrons and a photonic cavity, Nature **582**, 50 (2020).

[25] N. V. Sapra, K. Y. Yang, D. Vercruysse, K. J. Leedle, D. S. Black, R. J. England, L. Su, R. Trivedi, Y. Miao, O. Solgaard, R. L. Byer, and J. Vučković, On-chip integrated laser-driven particle accelerator, Science **367**, 79 (2020).

[26] Y. Kurman, R. Dahan, H. H. Sheinfux, K. Wang, M. Yannai, Y. Adiv, O. Reinhardt, L. H. G. Tizei, S. Y. Woo, J. Li, J. H. Edgar, M. Kociak, F. H. L. Koppens, and I. Kaminer, Spatiotemporal imaging of 2D polariton wave packet dynamics using free electrons, Science **372**, 1181 (2021).

[27] M. Liebtrau, M. Sivis, A. Feist, H. Lourenço-Martins, N. Pazos-Pérez, R. A. Alvarez-Puebla, F. J. G. de Abajo, A. Polman, and C. Ropers, Spontaneous and stimulated electron–photon interactions in nanoscale plasmonic near fields, Light: Sci. Appl. **10**, 82 (2021).

[28] M. Kociak and L. Zagonel, Cathodoluminescence in the scanning transmission electron microscope, Ultramicroscopy **176**, 112 (2017).

[29] A. Polman, M. Kociak, and F. J. García de Abajo, Electron-beam spectroscopy for nanophotonics, Nat. Mater. **18**, 1158 (2019).

[30] F. J. García de Abajo and V. Di Giulio, ACS Photonics, acsphotonics.0c01950 (2021), ArXiv:2010.13510.

[31] O. Kfir, H. Lourenço-Martins, G. Storeck, M. Sivis, T. R. Harvey, T. J. Kippenberg, A. Feist, and C. Ropers, Controlling free electrons with optical whispering-gallery modes, Nature **582**, 46 (2020).

[32] N. Müller, V. Hock, H. Koch, N. Bach, C. Rathje, and S. Schäfer, ACS Photonics, acsphotonics.1c00456 (2021), ArXiv:2103.13276.

[33] Y. Auad, C. Hamon, M. Tencé, H. Lourenço-Martins, V. Mkhitaryan, O. Stéphan, F. J. García de Abajo, L. H. G. Tizei, and M. Kociak, Unveiling the coupling of single metallic nanoparticles to whispering-gallery microcavities, Nano Lett. **22**, 319 (2022).

[34] E. Pomarico, I. Madan, G. Berruto, G. M. Vanacore, K. Wang, I. Kaminer, F. J. García de Abajo, and F. Carbone, meV resolution in laser-assisted energy-filtered transmission electron microscopy, ACS Photon. **5**, 759 (2018).

[35] J.-W. Henke, A. S. Raja, A. Feist, G. Huang, G. Arend, Y. Yang, F. J. Kappert, R. N. Wang, M. Möller, J. Pan, J. Liu, O. Kfir, C. Ropers, and T. J. Kippenberg, Integrated photonics enables continuous-beam electron phase modulation, Nature **600**, 653 (2021).

[36] R. Shiloh, J. Illmer, T. Chlouba, P. Yousefi, N. Schönenberger, U. Niedermayer, A. Mittelbach, and P. Hommelhoff, Electron phase-space control in photonic chip-based particle acceleration, Nature **597**, 498 (2021).

[37] O. Kfir, Entanglements of Electrons and Cavity Photons in the Strong-Coupling Regime, Phys. Rev. Lett. **123**, 103602 (2019).

[38] V. Di Giulio, M. Kociak, and F. J. G. de Abajo, Probing quantum optical excitations with fast electrons, Optica **6**, 1524 (2019).

[39] A. Ben Hayun, O. Reinhardt, J. Nemirovsky, A. Karnieli, N. Rivera, and I. Kaminer, Shaping quantum photonic states using free electrons, Sci. Adv. **7**, eabe4270 (2021).

[40] S. V. Yalunin, A. Feist, and C. Ropers, Tailored high-contrast attosecond electron pulses for coherent excitation and scattering, Phys. Rev. Res. **3**, L032036 (2021).

[41] R. Dahan, G. Baranes, A. Gorlach, R. Ruimy, N. Rivera, and I. Kaminer, Creation of optical cat and GKP states using shaped free electrons (2022).

[42] M. Kozák, P. Beck, H. Deng, J. McNeur, N. Schönenberger, C. Gaida, F. Stutzki, M. Gebhardt, J. Limpert, A. Ruehl, I. Hartl, O. Solgaard, J. S. Harris, R. L. Byer, and P. Hommelhoff, Acceleration of sub-relativistic electrons with an evanescent optical wave at a planar interface, Opt. Express **25**, 19195 (2017).

[43] R. Dahan, S. Nehemia, M. Shentcis, O. Reinhardt, Y. Adiv, X. Shi, O. Be'er, M. H. Lynch, Y. Kurman, K. Wang, and I. Kaminer, Resonant phase-matching between a light wave and a free-electron wavefunction, Nat. Phys. **16**, 1123 (2020).

[44] D. K. Gramotnev and S. I. Bozhevolnyi, Plasmonics beyond the diffraction limit, Nat. Photon. **4**, 83 (2010).

[45] F. J. García de Abajo and A. Howie, Relativistic Electron Energy Loss and Electron-Induced Photon Emission in Inhomogeneous Dielectrics, Phys. Rev. Lett. **80**, 5180 (1998).

[46] A. Feist, G. Huang, G. Arend, Y. Yang, J.-W. Henke, A. S. Raja, F. J. Kappert, R. N. Wang, H. Lourenço-Martins, Z. Qiu, J. Liu, O. Kfir, T. J. Kippenberg, and C. Ropers, Cavity-mediated electron-photon pairs, Science **377**, 777 (2022).

[47] M. H. P. Pfeiffer, C. Herkommer, J. Liu, H. Guo, M. Karpov, E. Lucas, M. Zervas, and T. J. Kippenberg, Octave-spanning dissipative Kerr soliton frequency combs in Si_3N_4 microresonators, Optica **4**, 684 (2017).

[48] G. Moille, X. Lu, J. Stone, D. Westly, and K. Srinivasan, Arbitrary microring dispersion engineering for ultrabroad frequency combs: Photonic crystal microring design based on Fourier synthesis (2022).

[49] J. Liu, G. Huang, R. N. Wang, J. He, A. S. Raja, T. Liu, N. J. Engelsen, and T. J. Kippenberg, High-yield, wafer-scale fabrication of ultralow-loss, dispersion-engineered silicon nitride photonic circuits, Nat. Commun. **12**, 2236 (2021).

[50] V. R. Almeida, R. R. Panepucci, and M. Lipson, Nanotaper for compact mode conversion, Opt. Lett. **28**, 1302 (2003).

[51] W. Bogaerts, D. Pérez, J. Capmany, D. A. B. Miller, J. Poon, D. Englund, F. Morichetti, and A. Melloni, Programmable photonic circuits, Nature **586**, 207 (2020).

[52] A. Li and Y. Fainman, On-chip spectrometers using stratified waveguide filters, Nat. Commun. **12**, 2704 (2021).

[53] F. Najafi, J. Mower, N. C. Harris, F. Bellei, A. Dane, C. Lee, X. Hu, P. Kharel, F. Marsili, S. Assefa, K. K. Berggren, and D. Englund, On-chip detection of non-classical light by scalable integration of single-photon detectors, Nat. Commun. **6**, 5873 (2015).

[54] A. Politi, M. J. Cryan, J. G. Rarity, S. Yu, and J. L. O'Brien, Silica-on-silicon waveguide quantum circuits, Science **320**, 646 (2008).

[55] O. Kfir, V. Di Giulio, F. J. G. de Abajo, and C. Ropers, Optical coherence transfer mediated by free electrons, Sci. Adv. **7**, eabf6380 (2021).

[56] X. Bendaña, A. Polman, and F. J. García de Abajo, Single-photon generation by electron beams, Nano Lett. **11**, 5099 (2011).

[57] Y. Adiv, H. Hu, S. Tsesses, R. Dahan, K. Wang, Y. Kurman, A. Gorlach, H. Chen, X. Lin, G. Bartal, and I. Kaminer, Observation of 2D Cherenkov Radiation, Phys. Rev. X **13**, 011002 (2023).

[58] A. Rényi, *et al.*, in *Proceedings of the fourth Berkeley symposium on mathematical statistics and probability*, 547-561 (Berkeley, California, USA, 1961).

[59] P. Milonni, *The Quantum Vacuum: An Introduction to Quantum Electrodynamics* (Academic Press, Boston, 1994).

[60] B. Barwick and H. Batelaan, Aharonov–Bohm phase shifts induced by laser pulses, New J. Phys. **10**, 083036 (2008).

[61] Y. Pan and A. Gover, Spontaneous and stimulated emissions of a preformed quantum free-electron wave function, Phys. Rev. A **99**, 052107 (2019).

[62] Y. Pan and A. Gover, Beyond Fermi's golden rule in free-electron quantum electrodynamics: acceleration/radiation correspondence, New J. Phys. **23**, 063070 (2021).

[63] A. Karnieli, N. Rivera, A. Arie, and I. Kaminer, The coherence of light is fundamentally tied to the quantum coherence of the emitting particle, Sci. Adv. **7**, eabf8096 (2021).

[64] S. V. Yalunin, A. Feist, and C. Ropers, Tailored high-contrast attosecond electron pulses for coherent excitation and scattering, Phys. Rev. Res. **3**, L032036 (2021).

[65] Y. Morimoto and P. Baum, Diffraction and microscopy with attosecond electron pulse trains, Nat. Phys. **14**, 252 (2018).

[66] N. Schönenberger, A. Mittelbach, P. Yousefi, J. McNeur, U. Niedermayer, and P. Hommelhoff, Generation and Characterization of Attosecond Microbunched Electron Pulse Trains via Dielectric Laser Acceleration, Phys. Rev. Lett. **123**, 264803 (2019).

[67] O. Krivanek, N. Dellby, J. Hachtel, J.-C. Idrobo, M. Hotz, B. Plotkin-Swing, N. Bacon, A. Bleloch, G. Corbin, M. Hoffman, C. Meyer, and T. Lovejoy, Progress in ultra-high energy resolution EELS, Ultramicroscopy **203**, 60 (2019).

[68] H. T. Dung, L. Knöll, and D.-G. Welsch, Three-dimensional quantization of the electromagnetic field in dispersive and absorbing inhomogeneous dielectrics, Phys. Rev. A **57**, 3931 (1998).

[69] R. A. Vicencio, C. Cantillano, L. Morales-Inostroza, B. Real, C. Mejía-Cortés, S. Weimann, A. Szameit, and M. I. Molina, Observation of Localized States in Lieb Photonic Lattices, Phys. Rev. Lett. **114**, 245503 (2015).

[70] S. Mukherjee, A. Spracklen, D. Choudhury, N. Goldman, P. Öhberg, E. Andersson, and R. R. Thomson, Observation of a Localized Flat-Band State in a Photonic Lieb Lattice, Phys. Rev. Lett. **114**, 245504 (2015).

[71] Y. Yang, C. Roques-Carmes, S. E. Kooi, H. Tang, J. Beroz, E. Mazur, I. Kaminer, J. D. Joannopoulos, and M. Soljačić, Photonic flatband resonances for free-electron radiation, Nature **613**, 42 (2023).

[72] E. Lucas, S.-P. Yu, T. C. Briles, D. R. Carlson, and S. B. Papp, Tailoring microcombs with inverse-designed, meta-dispersion microresonators (2022).

[73] E. M. Purcell, in *Confined Electrons and Photons: New Physics and Applications*, edited by E. Burstein and C. Weisbuch (Springer US, Boston, MA, 1995), p. 839.

[74] M. W. Mitchell, J. S. Lundeen, and A. M. Steinberg, Super-resolving phase measurements with a multiphoton entangled state, Nature **429**, 161 (2004).

[75] F. Hasselbach, Progress in electron- and ion-interferometry, Rep. Prog. Phys. **73**, 016101 (2009).

[76] A. O. C. Davis, V. Thiel, M. Karpiński, and B. J. Smith, Measuring the Single-Photon Temporal-Spectral Wave Function, Phys. Rev. Lett. **121**, 083602 (2018).

[77] U. Niedermayer, T. Egenolf, and O. Boine-Frankenheim, Three Dimensional Alternating-Phase Focusing for Dielectric-Laser Electron Accelerators, Phys. Rev. Lett. **125**, 164801 (2020).

[78] O. Krivanek, N. Dellby, and A. Lupini, Towards sub-Å electron beams, Ultramicroscopy **78**, 1 (1999).

[79] K. J. Resch, K. L. Pregnell, R. Prevedel, A. Gilchrist, G. J. Pryde, J. L. O'Brien, and A. G. White, Time-Reversal and Super-Resolving Phase Measurements, Phys. Rev. Lett. **98**, 223601 (2007).

[80] O. Reinhardt and I. Kaminer, Theory of shaping electron wavepackets with light, ACS Photon. **7**, 2859 (2020).

[81] A. Feist, N. Bach, N. Rubiano da Silva, T. Danz, M. Möller, K. E. Priebe, T. Domröse, J. G. Gatzmann, S. Rost, J. Schauss, S. Strauch, R. Bormann, M. Sivis, S. Schäfer, and C. Ropers, Ultrafast transmission electron microscopy using a laser-driven field emitter: Femtosecond resolution with a high coherence electron beam, Ultramicroscopy **176**, 63 (2017).

[82] P. Baum, On the physics of ultrashort single-electron pulses for time-resolved microscopy and diffraction, Chem. Phys. **423**, 55 (2013).

[83] U. Leonhardt, Quantum-State Tomography and Discrete Wigner Function, Phys. Rev. Lett. **74**, 4101 (1995).

[84] M. G. Paris, Displacement operator by beam splitter, Phys. Lett. A **217**, 78 (1996).

[85] M. Eaton, A. Hossameldin, R. J. Birrittella, P. M. Alsing, C. C. Gerry, H. Dong, C. Cuevas, and O. Pfister, Nat. Photon. (2022).

[86] R. Cheng, Y. Zhou, S. Wang, M. Shen, T. Taher, and H. X. Tang, Nat. Photon. (2022).

[87] S. Daiss, S. Welte, B. Hacker, L. Li, and G. Rempe, Single-Photon Distillation via a Photonic Parity Measurement Using Cavity QED, Phys. Rev. Lett. **122**, 133603 (2019).

[88] D. Najer, I. Söllner, P. Sekatski, V. Dolique, M. C. Löbl, D. Riedel, R. Schott, S. Starosielec, S. R. Valentin, A. D. Wieck, N. Sangouard, A. Ludwig, and R. J. Warburton, A gated quantum dot strongly coupled to an optical microcavity, Nature **575**, 622 (2019).

[89] G. S. Thekkadath, B. A. Bell, I. A. Walmsley, and A. I. Lvovsky, Engineering Schrödinger cat states with a photonic even-parity detector, Quantum **4**, 239 (2020).

[90] E. Bimbard, R. Boddeda, N. Vitrant, A. Grankin, V. Parigi, J. Stanojevic, A. Ourjoumtsev, and P. Grangier, Homodyne Tomography of a Single Photon Retrieved on Demand from a Cavity-Enhanced Cold Atom Memory, Phys. Rev. Lett. **112**, 033601 (2014).

[91] A. Tikan, J. Riemensberger, K. Komagata, S. Hönl, M. Churaev, C. Skehan, H. Guo, R. N. Wang, J. Liu, P. Seidler, and T. J. Kippenberg, Emergent nonlinear phenomena in a driven dissipative photonic dimer, Nat. Phys. **17**, 604 (2021).

[92] T. J. Kippenberg, A. L. Gaeta, M. Lipson, and M. L. Gorodetsky, Dissipative Kerr solitons in optical microresonators, Science **361**, eaan8083 (2018).

[93] M. Zhang, B. Buscaino, C. Wang, A. Shams-Ansari, C. Reimer, R. Zhu, J. M. Kahn, and M. Lončar, Broadband electro-optic frequency comb generation in a lithium niobate microring resonator, Nature **568**, 373 (2019).

[94] A. M. Weiner, Femtosecond pulse shaping using spatial light modulators, Rev. Sci. Instrum. **71**, 1929 (2000).

[95] M. Gao, Q.-F. Yang, Q.-X. Ji, H. Wang, L. Wu, B. Shen, J. Liu, G. Huang, L. Chang, W. Xie, S.-P. Yu, S. B. Papp, J. E. Bowers, T. J. Kippenberg, and K. J. Vahala, Probing material absorption and optical nonlinearity of integrated photonic materials, Nat. Commun. **13**, 3323 (2022).

[96] M. W. Puckett, K. Liu, N. Chauhan, Q. Zhao, N. Jin, H. Cheng, J. Wu, R. O. Behunin, P. T. Rakich, K. D. Nelson, and D. J. Blumenthal, 422 Million intrinsic quality factor planar integrated all-waveguide resonator with sub-MHz linewidth, Nat. Commun. **12**, 934 (2021).

[97] A. Shams-Ansari, G. Huang, L. He, Z. Li, J. Holzgrafe, M. Jankowski, M. Churaev, P. Kharel, R. Cheng, D. Zhu, N.

Sinclair, B. Desiatov, M. Zhang, T. J. Kippenberg, and M. Lončar, Reduced material loss in thin-film lithium niobate waveguides, APL Photon. **7**, 081301 (2022).
[98] R. Sahu, W. Hease, A. Rueda, G. Arnold, L. Qiu, and J. M. Fink, Quantum-enabled operation of a microwave-optical interface, Nat. Commun. **13**, 1276 (2022).
[99] L. Fan, C.-L. Zou, R. Cheng, X. Guo, X. Han, Z. Gong, S. Wang, and H. X. Tang, Superconducting cavity electro-optics: A platform for coherent photon conversion between superconducting and photonic circuits, Sci. Adv. **4**, eaar4994 (2018).
[100] C. K. Law and J. H. Eberly, Arbitrary Control of a Quantum Electromagnetic Field, Phys. Rev. Lett. **76**, 1055 (1996).
[101] M. Hofheinz, H. Wang, M. Ansmann, R. C. Bialczak, E. Lucero, M. Neeley, A. D. O'Connell, D. Sank, J. Wenner, J. M. Martinis, and A. N. Cleland, Synthesizing arbitrary quantum states in a superconducting resonator, Nature **459**, 546 (2009).
[102] D. I. Schuster, A. A. Houck, J. A. Schreier, A. Wallraff, J. M. Gambetta, A. Blais, L. Frunzio, J. Majer, B. Johnson, M. H. Devoret, S. M. Girvin, and R. J. Schoelkopf, Resolving photon number states in a superconducting circuit, Nature **445**, 515 (2007).
[103] Y.-H. Kim, R. Yu, S. P. Kulik, Y. Shih, and M. O. Scully, Delayed 'Choice' Quantum Eraser, Phys. Rev. Lett. **84**, 1 (2000).
[104] P. Kruit, R. Hobbs, C.-S. Kim, Y. Yang, V. Manfrinato, J. Hammer, S. Thomas, P. Weber, B. Klopfer, C. Kohstall, T. Juffmann, M. Kasevich, P. Hommelhoff, and K. Berggren, Designs for a quantum electron microscope, Ultramicroscopy **164**, 31 (2016).
[105] H. Okamoto, A universal quantum electron microscope for phase objects: Hardware designs and possible applications (2022).
[106] N. Talebi, Electron-light interactions beyond the adiabatic approximation: recoil engineering and spectral interferometry, Adv. Phys.: X **3**, 1499438 (2018).
[107] W. J. Tomlinson, R. H. Stolen, and C. V. Shank, Compression of optical pulses chirped by self-phase modulation in fibers, J. Opt. Soc. Am. B **1**, 139 (1984).
[108] E. Nitiss, J. Hu, A. Stroganov, and C.-S. Brès, Optically reconfigurable quasi-phase-matching in silicon nitride microresonators, Nat. Photon. **16**, 134 (2022).
[109] L. Wang, L. Chang, N. Volet, M. H. P. Pfeiffer, M. Zervas, H. Guo, T. J. Kippenberg, and J. E. Bowers, Frequency comb generation in the green using silicon nitride microresonators, Laser Photon. Rev. **10**, 631 (2016).
[110] A. Siddharth, T. Wunderer, G. Lihachev, A. S. Voloshin, C. Haller, R. N. Wang, M. Teepe, Z. Yang, J. Liu, J. Riemensberger, N. Grandjean, N. Johnson, and T. J. Kippenberg, Near ultraviolet photonic integrated lasers based on silicon nitride, APL Photon. **7**, 046108 (2022).
[111] M. A. Tran, C. Zhang, T. J. Morin, L. Chang, S. Barik, Z. Yuan, W. Lee, G. Kim, A. Malik, Z. Zhang, J. Guo, H. Wang, B. Shen, L. Wu, K. Vahala, J. E. Bowers, H. Park, and T. Komljenovic, Extending the spectrum of fully integrated photonics to submicrometre wavelengths, Nature **610**, 54 (2022).
[112] Z. Zhao, X.-Q. Sun, and S. Fan, Quantum Entanglement and Modulation Enhancement of Free-Electron–Bound-Electron Interaction, Phys. Rev. Lett. **126**, 233402 (2021).
[113] A. Gover and A. Yariv, Free-Electron–Bound-Electron Resonant Interaction, Phys. Rev. Lett. **124**, 064801 (2020).
[114] M. Karpov, H. Guo, A. Kordts, V. Brasch, M. H. P. Pfeiffer, M. Zervas, M. Geiselmann, and T. J. Kippenberg, Raman Self-Frequency Shift of Dissipative Kerr Solitons in an Optical Microresonator, Phys. Rev. Lett. **116**, 103902 (2016).
[115] O. L. Krivanek, T. C. Lovejoy, N. Dellby, T. Aoki, R. W. Carpenter, P. Rez, E. Soignard, J. Zhu, P. E. Batson, M. J. Lagos, R. F. Egerton, and P. A. Crozier, Vibrational spectroscopy in the electron microscope, Nature **514**, 209 (2014).
[116] K. Venkatraman, B. D. A. Levin, K. March, P. Rez, and P. A. Crozier, Vibrational spectroscopy at atomic resolution with electron impact scattering, Nat. Phys. **15**, 1237 (2019).
[117] F. Hofer, F. P. Schmidt, W. Grogger, and G. Kothleitner, Fundamentals of electron energy-loss spectroscopy, IOP Conf. Seri.: Mater. Sci. Eng. **109**, 012007 (2016).
[118] V. Di Giulio, O. Kfir, C. Ropers, and F. J. García de Abajo, ACS Nano, acsnano.1c00549 (2021), ArXiv:2101.07748.
[119] T. Gruner and D.-G. Welsch, Green-function approach to the radiation-field quantization for homogeneous and inhomogeneous Kramers-Kronig dielectrics, Phys. Rev. A **53**, 1818 (1996).
[120] J. Feist, A. I. Fernández-Domínguez, and F. J. García-Vidal, Macroscopic QED for quantum nanophotonics: emitter-centered modes as a minimal basis for multiemitter problems, Nanophotonics **10**, 477 (2021).
[121] R. H. Ritchie and A. Howie, Inelastic scattering probabilities in scanning transmission electron microscopy, Philos. Mag. A **58**, 753 (1988).
[122] R. H. Ritchie, Plasma losses by fast electrons in thin films, Phys. Rev. **106**, 874 (1957).
[123] R. J. Glauber and M. Lewenstein, Quantum optics of dielectric media, Phys. Rev. A **43**, 467 (1991).
[124] K. J. Blow, R. Loudon, S. J. D. Phoenix, and T. J. Shepherd, Continuum fields in quantum optics, Phys. Rev. A **42**, 4102 (1990).
[125] B. Brecht, D. V. Reddy, C. Silberhorn, and M. G. Raymer, Photon Temporal Modes: A Complete Framework for Quantum Information Science, Phys. Rev. X **5**, 041017 (2015).
[126] M. G. Raymer and I. A. Walmsley, Temporal modes in quantum optics: then and now, Phys. Scr. **95**, 064002 (2020).
[127] C. W. Gardiner and M. J. Collett, Input and output in damped quantum systems: Quantum stochastic differential equations and the master equation, Phys. Rev. A **31**, 3761 (1985).
[128] A. I. Lvovsky, H. Hansen, T. Aichele, O. Benson, J. Mlynek, and S. Schiller, Quantum State Reconstruction of the Single-Photon Fock State, Phys. Rev. Lett. **87**, 050402 (2001).
[129] T. Tyc and B. C. Sanders, Operational formulation of homodyne detection, J. Phys. A: Math. Gen. **37**, 7341 (2004).

[130] F. Soto-Eguibar and H. M. Moya-Cessa, Harmonic oscillator position eigenstates via application of an operator on the vacuum, Revista Mexicana de Física E **59**, 122 (2013).

[131] A. P. Higginbotham, P. S. Burns, M. D. Urmey, R. W. Peterson, N. S. Kampel, B. M. Brubaker, G. Smith, K. W. Lehnert, and C. A. Regal, Harnessing electro-optic correlations in an efficient mechanical converter, Nat. Phys. **14**, 1038 (2018).

[132] C. Javerzac-Galy, K. Plekhanov, N. R. Bernier, L. D. Toth, A. K. Feofanov, and T. J. Kippenberg, On-chip microwave-to-optical quantum coherent converter based on a superconducting resonator coupled to an electro-optic microresonator, Phys. Rev. A **94**, 053815 (2016).

[133] W. B. Case, M. Tomandl, S. Deachapunya, and M. Arndt, Realization of optical carpets in the Talbot and Talbot-Lau configurations, Opt. Express **17**, 20966 (2009).